Accelerated Particle Composition and Energetics and Ambient Abundances from Gamma-Ray Spectroscopy of the 1991 June 4 Solar Flare

R. J. Murphy, G. H. Share, J. E. Grove, W. N. Johnson, R. L. Kinzer, J. D. Kurfess and M. S. Strickman
E.O. Hulburt Center for Space Research, Code 7650, Naval Research Lab., Washington, DC 20375, U.S.A.

G. V. Jung
Universities Space Research Association, Washington, DC 20024, U.S.A.
Accepted for publication in the Astrophysical Journal

ABSTRACT

The Oriented Scintillation Spectrometer Experiment (OSSE) on board the COMPTON Gamma Ray Observatory observed the 1991 June 4 X12+ solar flare, one of the most intense nuclear gamma-ray line flares observed to date. Using these OSSE observations, we have derived time profiles of the various components of gamma-ray emission and obtained information about the accelerated particle spectra and composition and about the ambient plasma at the flare site. The main results are: (1) the nuclear reactions associated with the impulsive phase of the flare continued for at least 2 hours and resulted from ions that were probably continuously accelerated rather than impulsively accelerated and trapped; (2) the total energy in these accelerated ions exceeded the energy in >0.1 MeV electrons; (3) the accelerated α/proton ratio was closer to 0.5 than to 0.1; (4) there is evidence for a decrease of the accelerated heavy ion-to-proton ratio as the flare progressed (5) there is evidence for a temporal change in the composition of the flare plasma; (6) the ratio of electron bremsstrahlung to the flux in narrow γ-ray lines decreased as the flare progressed; (7) the high-energy (>16 MeV) component of the electron spectrum was much more impulsive than the lower-energy ~MeV component; (8) a model-dependent upper limit of 2.3 $\times$ 10^{-5} was obtained for the photospheric ^{3}He/H abundance ratio; and (9) energetic ions may have been present for several hours prior to and following the impulsive phase of the flare.

Subject headings: Sun: flares — Sun: X-rays, gamma rays — Sun: abundances — acceleration of particles

1. INTRODUCTION

Prior to the launch of the *COMPTON Gamma Ray Observatory* (*CGRO*), most solar γ-ray line measurements had been made with the *Solar Maximum Mission*, *Hinotori*, *Yohkoh*, and *GRANAT* γ-ray spectrometers (e.g., Chupp 1987; Yoshimori 1989; Yoshimori 1994; Vilmer 1994). With the launch of the *CGRO* in April of 1991, a new resource for high-energy solar measurements became available. In early June, less than two months after launch, active region 6659 rotated onto the disk and produced some of the largest X-ray flares ever recorded. On June 1, AR 6659 appeared at the east limb and produced an X12+ flare. The peak of this flare was missed by the *CGRO* instruments because the satellite was in the South Atlantic Anomaly (SAA), but it was observed by the PHEBUS experiment on *GRANAT* (Barat *et al.* 1994). As there was a high probability for subsequent intense flares, a solar Target of Opportunity was declared for the Oriented Scintillation Spectrometer Experiment (OSSE) on *CGRO* which is sensitive to γ rays from 0.04 to >150 MeV. The Sun was then observed for roughly 30 – 40 minutes during each orbit and, on June 4, AR 6659 produced a second X12+ flare while OSSE was viewing the Sun. The flare was one of the most intense nuclear γ-ray line flares observed to date; most instruments, from the soft X-ray to the γ-ray bands, saturated at its peak. The NOAA *Solar-Geophysical Data Comprehensive Report* gives the Hα flare location as N30E70. This location corresponds to a heliocentric angle of 74.5° at the time of the flare.

Based on the count rate of $\gtrsim$ 20 keV X-rays observed from the June 4 flare by the Solar X-Ray/Cosmic Gamma-Ray Burst Experiment on Ulysses, Kane *et al.* (1995) derived a peak >20 keV electron injection rate of 5.7×10^{38} electrons s^{-1} and an energy dissipation rate of 2.5×10^{31} ergs s^{-1}. Given its long duration, they pointed out that the material and energy resources of the active region appeared to be inadequate for the production of such a flare. Ramaty *et al.* (1994) used data from the BATSE Charged Particle Detectors (CPD; the only *CGRO* detectors sensitive to ~MeV γ rays not saturated at the peak of the flare) to monitor the electron bremsstrahlung time profile and estimate the magnetic field strength in the coronal portion of the flare loop. Using the EGRET Total Absorption Shower Counter (TASC), Bertsch *et al.* (1997) measured γ-ray line fluxes starting after the impulsive peak of the flare. The flare also produced >100 MeV neutrons (Takahashi *et al.* 1991; Muraki *et al.* 1992; Struminsky *et al.* 1994) and possibly even >10 GeV neutrons (Chiba *et al.* 1992). Energetic particles from the flare were observed in interplanetary space by the EPAC experiment on Ulysses (McDonald *et al.* 1995) and the flare was observed at 17, 35 and 80 GHz by radiometers at the Nobeyama Radio Observatory in Japan (Ramaty *et al.* 1994). The combined interplanetary modulation effects of the June 4 flare and the other intense June flares resulted in the lowest celestial cosmic-ray flux at earth in almost 40 years (Webber and Lockwood 1993; Van Allen 1993) and strong radio emission generated

by the associated interplanetary shock at the heliopause (Gurnett *et al.* 1993).

In this paper we present OSSE observations of the June 4 flare over a broad spectral range from 0.1 to $\sim$ 100 MeV. Observations were obtained of the rise (3:37 UT), peak (3:52 UT), and decay of the event. The decay was observed over the next several orbits, interrupted only by spacecraft night. Plotted in Figure 1 are the intensity profiles of this flare as monitored by live-time corrected OSSE rates above 0.1 MeV, between 1 and 10 MeV, and above 16 MeV during the first orbit. The peak of the γ-ray intensity and the time when the OSSE detectors were repointed to the secondary target just prior to satellite night are indicated by dotted lines. For comparison, the *GOES* 1 – 8 Å X-ray profile is also plotted. All of the rates (with the exception of the >16 MeV band) exhibited saturation at the peak of the emission. As discussed below, the >0.1 MeV γ-ray flux is dominated by bremsstrahlung of >0.1 MeV electrons, the 1 –10 MeV flux is a combination of bremsstrahlung and nuclear line emission and the >16 MeV flux is probably also bremsstrahlung but of high-energy electrons. Each of these emissions has a unique time profile. The increase in the >16 MeV rates after 3.7 hr UT is due to the arrival at Earth of flare-produced neutrons. The high energy emissions have been discussed previously (DelSignore 1995). Here, we concentrate primarily on measurements of nuclear lines and continuum between 0.1 and 9 MeV.

We have fit the OSSE data with a multi-component model of solar flare γ-ray spectra and produced time profiles of various γ-ray line intensities throughout the flare with a time resolution as short as 8.2 s. Fits of the 2.223 MeV neutron-capture line and narrow and broad nuclear de-excitation lines provide information on the ambient plasma at the flare site and the accelerated-ion spectrum. These are the only complete measurements of the ion-induced emissions from this flare. Using the measured electron bremsstrahlung, information on the accelerated electrons has also been obtained. Preliminary results from analyses of the OSSE data have been reported previously (Murphy *et al.* 1993b; Murphy *et al.* 1993a; Murphy *et al.* 1994; Murphy *et al.* 1996). In §2 we briefly discuss γ-ray production in solar flares. In §3 we describe the OSSE instrument, data collection modes, and techniques for analyzing data from intense flares. The spectroscopic and temporal observations are presented in §4 and the implications for solar flare models are discussed in §5.

2. GAMMA RAY PRODUCTION IN SOLAR FLARES

Interactions of flare-accelerated protons and nuclei with the ambient solar atmosphere produce neutrons, γ-ray lines and continuum emission and have been studied in detail

(e.g., Ramaty and Murphy 1987; Ramaty and Mandzhavidze 1994; Hudson and Ryan 1995). The principal mechanisms for the production of γ-ray lines are nuclear de-excitation, neutron capture and positron annihilation. The nuclear de-excitation spectrum consists of narrow lines ($\sim$2% full width at half maximum (FWHM)), resulting from protons and α particles interacting with the ambient gas, and broad lines ($\sim$20% FWHM), resulting from accelerated carbon and heavier nuclei interacting with ambient hydrogen and helium. Capture of flare-produced neutrons on ambient hydrogen in the photosphere produces a strong line at 2.223 MeV. Nuclear reactions also produce radioactive nuclei and charged pions whose decay result in positron emission. The positrons annihilate to produce a line at 0.511 MeV and a 3-photon positronium continuum. The narrow nuclear de-excitation lines and the 2.223 and 0.511 MeV lines are superposed on a continuum composed of the broad nuclear de-excitation lines and bremsstrahlung from primary electrons.

The most important narrow nuclear de-excitation lines in solar flares are at 0.429 and 0.478 MeV (^{7}Be and ^{7}Li), 0.847 MeV (^{56}Fe), 1.238 MeV (^{56}Fe), 1.369 MeV (^{24}Mg), 1.634 MeV (^{20}Ne), 1.778 MeV (^{28}Si), 4.439 MeV (^{12}C), and 6.129 MeV (^{16}O) (Kozlovsky and Ramaty 1974; Ramaty, Kozlovsky and Lingenfelter 1979). Two additional features appear in solar flare γ-ray spectra at $\sim$5.3 and $\sim$7 MeV that are complexes of lines resulting primarily from inelastic excitation and spallation of ^{14}N and ^{16}O. The narrow lines are due mostly to accelerated protons with kinetic energies of 5 – 30 MeV and α particles with energies of 2 – 10 MeV nucleon^{-1}. The relative strengths of the narrow lines primarily depend on the relative ambient-gas abundances, but they also are affected by the energy spectra of the accelerated particles. Because the 1.634 and 6.129 MeV lines of Ne and O are relatively strong and the energy dependencies of their production cross sections are distinctly different, they are particularly useful for measuring the spectral hardness of interacting accelerated particles (Share and Murphy 1995; Ramaty *et al.* 1995).

The neutrons producing the 2.223 MeV line from capture on H arise primarily from p-p, p-α and α-α particle interactions at energies of 30 – 100 MeV nucleon^{-1} (Wang and Ramaty 1974; Hua and Lingenfelter 1987). This line is therefore produced by higher-energy particles than those producing the de-excitation lines. Comparison of the 2.223 MeV line and de-excitation lines can thus provide spectral information about 10 – 100 MeV protons. The capture line is delayed by about 100 seconds because of the time required for the neutrons to slow down and be captured on ^{1}H. A competing capture reaction is ^{3}He(n,p)^{3}H which produces no radiation but shortens the delay of the 2.223 MeV line emission (Wang and Ramaty 1974). Measurements of the time profile of this line have been used to set constraints on the photospheric ^{3}He/H ratio (Prince *et al.* 1983; Hua and Lingenfelter 1987).

Ambient elemental abundances can be obtained by comparing γ-ray spectra calculated from measured nuclear cross sections and kinematic calculations with observed spectra (Ramaty, Kozlovsky and Lingenfelter 1975; Ramaty, Kozlovsky and Lingenfelter 1979; Murphy *et al.* 1991). Because most of the narrow lines are dominated by de-excitation from a single element, some information about relative ambient abundances can also be inferred directly from the narrow-line fluxes. Share and Murphy (1995) measured the fluxes of 10 narrow γ-ray lines in 19 X-class solar flares observed by the *Solar Maximum Mission*/Gamma Ray Spectrometer (*SMM*/GRS). Flare-to-flare variations in line fluxes suggested that the abundances of elements in the flare plasma are grouped with respect to first ionization potential (FIP): line fluxes from elements with similar FIP correlate well with one another. In contrast, the low-FIP to high-FIP line ratios were not consistent with a common value from flare to flare. The authors suggested that the line ratio variation may be due to ambient abundance variation rather than to spectral variation of the accelerated particles. Ramaty *et al.* (1995) used cross sections and kinematical calculations to determine the abundances for the *SMM*/GRS flares and showed that the composition of the flare plasma is close to coronal, although they did not rule out significant variability from flare to flare.

At photon energies below about 1 MeV the contribution of nuclear lines is small and continuum emission due to bremsstrahlung from directly accelerated electrons is expected to be the dominant source of photons. Similarly, at energies greater than about 8 MeV bremsstrahlung also dominates except when the accelerated-ion spectrum is very hard and the contribution from π-decay becomes important. Observations of solar hard X rays in the $\sim$20 to $\sim$400 keV region (e.g., by the *SMM* Hard X-Ray Burst Spectrometer; Dennis 1988) show that spectra in this energy range are usually well fit by power laws suggesting that the electrons are non-thermal, but in at least one flare a super-hot component (Lin *et al.* 1981) at energies $\lesssim$ 35 keV has been observed. Spectral fits to flare data obtained with the *SMM*/GRS (Vestrand *et al.* 1997) have also shown a power law to be an appropriate spectral form for the bremsstrahlung between 0.3 and 8 MeV in most flares, but a few flares were better fit when a broken power law or the sum of two power laws were used (see §4.1.1).

3. USING OSSE TO OBSERVE SOLAR FLARES

In this section we discuss the OSSE instrument, the configuration of the four detectors while observing flares during the June period, background subtraction and spectral fitting.

3.1. Instrument and Observing Configuration

The OSSE instrument is described by Johnson *et al.* (1993). A brief description of those aspects of the instrument relevant to solar observations is given here.

OSSE consists of four independently-oriented NaI/CsI phoswich scintillation detectors with both passive and active shielding for reducing background and defining its aperture (see Figure 2). The principal detector element is a 33 cm dia. phoswich. Pulses from photomultipliers optically coupled to the 10.2 cm thick NaI and 7.6 cm thick CsI crystals are separated by pulse-shape discrimination, providing a compact anticoincidence system for both charged particles and background γ rays. OSSE covers the energy range from 0.04 to >150 MeV and each detector has photopeak effective areas of $\sim$480 cm^2 and $\sim$170 cm^2 at 0.511 and 6 MeV, respectively. The energy resolution varies from detector to detector. At 6.1 MeV the fractional FWHM resolutions of the four detectors are 4%, 5%, 4%, and 7% (the poorer resolution of detector 4 occurred during growth of that NaI crystal). A tungsten collimator above the phoswich defines a $3.8^\circ \times 11.4^\circ$ FWHM geometrical field of view and a 3.5 in. thick NaI annulus completes the shielding. OSSE can detect γ-ray lines as weak as 1×10^{-3} photons cm^{-2} s^{-1} during a 1000-s exposure.

Each detector is mounted in an independent elevation-angle gimbal which allows 'scanning' through 192° of rotation. During the June 4 solar observations, the Sun was kept within 0.8° of the axes of detectors 1 and 3. In contrast, detectors 2 and 4 'chopped'; i.e., alternately pointed at and 4.5° off the Sun at 131.1-s intervals. Full spectra were accumulated from each detector at 8-s intervals. This observing sequence was optimized for relatively weak and short flares. During the viewing period, the Sun was in the direction of the spacecraft X-axis (see Figure 2). When pointed toward the Sun, Detectors 1 and 2 were partially shadowed ($\sim$13%) by Detectors 3 and 4 and their associated electronics.

The June 4 flare was so intense that it produced severe saturation effects in those detectors directly viewing the Sun. The large instrumental deadtimes produced by the intense flux of hard X-rays incident on the phoswich and annular shields were successfully monitored. However, pulse pile-up caused the pulse shapes from the NaI and CsI elements to become severely distorted. As a result, a large fraction of events no longer fell within the predefined NaI pulse-shape windows producing an effective deadtime for valid NaI events that could not be monitored.

Data from the single off-pointed detector were largely unaffected by pulse pile-up and pulse-shape distortion because the hard X-ray photons were absorbed in the shield and collimator. (In §3.3 we will show that during the 16 seconds at the peak of emission, even the off-pointed detector was probably suffering saturation effects.) This absorption

and scattering, however, prevents measurement of solar photons $\lesssim 1$ MeV. It also has significant effects on spectral measurements above 1 MeV, as shown in Figure 3 where the calculated responses to a unit flux of 6 MeV γ rays by a 'Sun-pointed' and by an 'off-pointed' OSSE detector are displayed. Although both the photopeak and 1^{st} escape peaks are reduced by about a factor of 4 for the off-pointed detector and the scattered radiation from the collimator dominates over the partially absorbed events in the phoswich below $\sim$3 MeV, these off-pointed spectra are the only reliable means of determining the fluxes of the neutron capture line and the de-excitation lines above 1 MeV during the first orbit. However, data from the three Sun-pointed detectors during orbits 2 and 3 can be used because the fluxes were low enough that there were no saturation effects. Moderately saturated data from the Sun-pointed detectors during the last 10 minutes of the first orbit have also been used. Because the flux of the 2.223 MeV line derived from Sun-pointed detector data agrees with that derived from off-pointed detector data during this time, we believe such data are reliable.

3.2. Background Subtraction

Detector background is not a significant contributor to the spectra during the more intense portions of the flare, but becomes an important factor at times late in the first orbit and in later orbits. Because the standard OSSE on-source minus off-source technique for background subtraction is not applicable for intense, rapidly-changing sources such as solar flares, an alternative scheme was developed. This procedure uses a background model and off-source measurements made by OSSE from launch through 1992 March 31 to obtain the dependence of individual background spectral parameters on the relevant orbital, detector, and environmental parameters. The procedure provides an estimate of the background for any observation, given only the measured parameters at that time and a nearby source-free background spectrum for normalization. For the June 4 flare, the normalization spectra for each detector were accumulated during solar quiet times (as monitored by *GOES*) of the orbit prior to the onset of the flare with the detectors viewing the Sun.

The background algorithm was verified by accumulating data at solar quiet times on an orbital basis for several days before and after the June 4 flare and fitting the spectra with the same photon model (see §3.3) used to fit flare spectra. Using the algorithm, residuals remained after background subtraction during orbits with an SAA exposure. Fortunately, the orbits associated with the June 4 flare (the flare orbit, the previous orbit, and the subsequent four orbits) were non-SAA orbits. For non-SAA times, the residuals were reasonably stable from orbit to orbit during a given day, being only slightly larger than expected from purely statistical causes. The magnitude of this systematic error due to

background subtraction was estimated by finding the additional error which, when added in quadrature with the statistical uncertainties, produced an acceptable χ^2 for a constant fit to each parameter over a full day. These systematic errors were then added in quadrature with the statistical uncertainties to obtain the total uncertainties during flare observations. The magnitudes of these systematic uncertainties were typically smaller than the statistical uncertainties of parameters derived from fits to either ~8-s or ~131.1-s data obtained from the off-pointed detectors during the first orbit. However, they became comparable to the statistical uncertainties derived from even Sun-pointed detectors when the rates dropped during the second and third orbits. Beginning on the second day following that of the normalization background spectrum, there were also larger day-to-day residuals remaining after background subtraction. These residuals add an uncertainty to our determination of absolute fluxes; we will consider these additional systematic uncertainties on a case by case basis.

Alternative techniques are being developed which will allow background-subtraction of transient sources such as solar flares with reduced systematic uncertainties. For example, providing a background estimate by using data obtained the day before and the day after during times with environmental conditions similar to the flare time is being studied. Such techniques will be applied in future analyses of flare data.

3.3. Spectral Fits

During the first orbit when the flare was intense, spectra from the detector pointed off the Sun are used in order to minimize saturation effects. Because of the low-energy attenuation, only data >1 MeV are used for fitting these spectra. The 8-s spectra were rebinned into broader energy bins to provide adequate numbers of counts for proper fitting at the highest energies where limited statistics can be a problem. Above 1 MeV, the rebinned widths are comparable to the FWHM of the detector spectral resolutions and we have demonstrated that the intensities of all line features in the spectra are faithfully obtained after this rebinning. In cases where energy-channel rebinning of an 8-s spectrum did not achieve a minimum of 15 counts in each channel, subsequent 8-s spectra were summed until such a minimum was achieved. Eight-second temporal resolution was achieved near the peak of the flare but accumulations of up to 40 s were required near the end of the first orbit. In addition, during the last 10 minutes of the first orbit and during the second and third orbits when saturation effects were minimal, spectral fits to 2-min accumulations of Sun-pointed detector data were also used and the spectral fits were performed above 0.1 MeV. Weighted means of the fits from the three Sun-pointed detectors are presented. There were no significant differences of the results from different detectors.

Spectral analyses were accomplished using a least-squares fitting technique: an assumed photon model was folded through the OSSE instrument response for the updated solar position, detector-by-detector, and compared to background-subtracted count spectra. The model parameters were adjusted until χ^2 was minimized. The fitting algorithm provided estimates of the uncertainties and the total uncertainty was then obtained by adding this statistical uncertainty in quadrature with the systematic uncertainty discussed in §3.2.

The model γ-ray spectrum used for fitting off-pointed >1 MeV spectra from the first orbit comprised a narrow 2.223 MeV neutron-capture line, the individual narrow nuclear de-excitation lines with energies >1 MeV (see §2), broad nuclear de-excitation lines, and an electron bremsstrahlung continuum. The model used for fitting Sun-pointed >0.1 MeV spectra also included a narrow 0.511 MeV positron-annihilation line, a positronium continuum, the α-α fusion lines, and nuclear de-excitation lines <1 MeV (see §2). The electron bremsstrahlung component for both Sun- and off-pointed data fitting was modeled by a single power-law with both its amplitude and exponent free to vary.

The widths of the positron annihilation, neutron capture and narrow nuclear de-excitation lines are expected to be narrower than the OSSE energy resolution. The positron annihilation and neutron capture lines are modeled as Gaussian profiles with central energies fixed at 0.511 and 2.223 MeV and widths fixed at 10 keV FWHM. The narrow nuclear de-excitation line energies and widths are fixed at the theoretical values listed by Murphy *et al.* (1990b). The α-α complex was modeled with one Gaussian, centered at 0.45 MeV and having a width of 100 keV FWHM. Only the amplitudes of these Gaussians were varied during fitting. The shape of the α-α complex can be used to infer information about the angular distribution of the interacting α particles (Kozlovsky and Ramaty 1977; Murphy *et al.* 1988; Murphy *et al.* 1990a; Share and Murphy 1997a). For the June 4 flare, this will be the subject of a separate study. For isotropic or fan-beam angular distributions of the accelerated particles (see Murphy *et al.* 1988), a simple Gaussian is adequate to model this complex for determining the flux of the line. Share and Murphy (1997a) have shown that spectra from most flares are better fit with such isotropic or fan-beam assumptions. The positron annihilation line will also be the subject of a separate study.

Because of difficulties fitting broad line features, the broad line component was not fit with individual Gaussians but with a *broad-line template*. The template, based on measurements of the 1981 April 27 *SMM*/GRS flare by Murphy *et al.* (1990b), is representative of flare spectra and consists of five broad Gaussians with fixed relative fluxes derived from new line measurements (Share and Murphy 1995) of the April 27 flare. The only free parameter is the amplitude of the template. In principle, fitting for the broad

component allows for the possibility of determining the ratio of accelerated heavy elements to accelerated protons during the flare. In practice, however, the *broad-line template* also accounts for proton-induced narrow lines unresolvable by the NaI detectors. In addition, separating the template from the bremsstrahlung continuum over the limited 1 – 9 MeV range used for the first-orbit fits is difficult. Fitting the Sun-pointed detector data down to 0.1 MeV allows a better determination of the bremsstrahlung power law since it dominates at these energies. Consequently, this allows a better determination of the broad component as well. Fitting with such a template does not allow a measurement of any variation of the accelerated-particle composition as the flare progressed. Such variation has been measured by Ramaty *et al.* (1997) for the 1991 June 1 flare observed by *GRANAT*/Phebus. Fitting with the template, though, gives a reasonable measure of an "average" flux of accelerated heavy elements.

Examples of data from both Sun- and off-pointed detectors, along with fits to the data using the models described above, are shown in Figure 4. Panel (a) shows an 8 s 1 – 9 MeV spectrum from an off-pointed detector accumulated shortly after the peak of the flare and rebinned into the larger energy bins. Panel (b) shows a 2-minute 0.1 – 9 MeV spectrum from a Sun-pointed detector accumulated late in the first orbit. The components of the models and the sources of various spectral features are identified in the Figure. Panel (b) shows that the assumption of a power law to model the electron bremsstrahlung component >0.1 MeV is justified. We note some excess of counts above the model at energies $\gtrsim$ 8 MeV, indicating more broad component than our model allows and/or a hard bremsstrahlung tail. We have shown that the derived fluxes of the narrow lines are unaffected by this discrepancy (see §4.1.1). This issue will be resolved when the OSSE high-energy spectral data are incorporated into the analysis.

Before presenting results of the spectral analysis, we wish to test whether any emission at the peak of the flare has been missed due to saturation of the off-pointed OSSE detector (Detector 2). The only *CGRO* detectors not saturated at energies <10 MeV during the flare were the BATSE CPDs. Shown in Figure 5 (thin histogram) is the time profile of the observed average count rate from the four Sun-facing BATSE CPDs; an estimate of the background, assumed to vary linearly with time, has been subtracted from the data. Ramaty *et al.* (1994) calculated an instrumental response and used these CPD data in their analysis of the June 4 flare. To compare with the BATSE data, the best-fitting OSSE high time resolution >1 MeV photon spectra obtained from the off-pointed detector are convolved with this BATSE CPD response to derive predicted CPD count rates (thick histogram shown in Figure 5). We note that using OSSE spectra derived from data >1 MeV only is valid for comparison because the CPD instrumental response falls rapidly below 1 MeV. The 1-sec BATSE count rates have been rebinned into the corresponding

OSSE accumulation intervals.

Figure 5 shows that, overall, the OSSE-derived CPD rates fall below the observed CPD rates by about a factor of 2.5. Also shown in Figure 5 (dotted histogram) is the OSSE derived count rate increased by a factor of 2.5 to normalize it to the observed BATSE CPD count rate on the rising and falling portions of the primary peak. The shape of the profile predicted from the OSSE data agrees reasonably well with the observed BATSE profile. (The higher relative rates of the CPD between the emission peaks as the emission falls could be due to improper subtraction of background; the assumption of a background time profile peaking during the flare, as suggested by the raw CPD count rates, can reduce this difference.) The overall discrepancy of a factor of 2.5 may be due to an underestimated CPD response function (Ramaty *et al.* 1994; we return to this issue in §5.2.4). After renormalization, the OSSE-derived CPD count rate falls short of the BATSE data during the two 8-s accumulations at the peak of the flare. This suggests that saturation effects have reduced the OSSE sensitivity by about a factor of two during these two intervals. The fluxes and fluences presented in this paper include a correction for radiation missed during these 16 seconds due to this saturation.

4. SPECTROSCOPIC OBSERVATIONS

In this section, spectral data accumulated in intervals as short as 8 s are used to obtain time profiles of nuclear de-excitation lines, the 2.223 MeV neutron capture line, and electron bremsstrahlung. We determine relative line intensities of the narrow γ-ray lines, derive the broad-line to narrow-line ratio, obtain spectral parameters of the accelerated ions and electrons, and discuss the accelerated α/proton ratio. A constraint on the photospheric ^{3}He/H abundance ratio is established. Techniques typically applied to the study of weak celestial sources are applied to search for nuclear emission occurring before and after the flare.

4.1. Narrow Nuclear Line Measurements and Ambient Abundance Estimates

4.1.1. Narrow Nuclear Line Measurements

Plotted in Figure 6 (histogram) is the three-orbit time profile of the flux observed in the sum of >1 MeV narrow de-excitation lines. The fluxes for the first orbit are derived from off-pointed detector data and the fluxes for the second and third orbits are derived from Sun-pointed detector data. During the third orbit the data have been summed into

14-minute accumulations to improve the statistics. The error bars represent the combined 1-σ statistical uncertainties and the systematic uncertainties associated with background subtraction found on orbital timescales (see §3.2). Nuclear interactions and the resultant γ-ray emission are seen to continue after the peak of the emission for at least 2 hr through the second orbit. Although there is statistical evidence for emission during the third orbit ($\sim$2.5 σ), the day to day systematic errors (see §3.2) weaken this conclusion. In §4.7 we will use the neutron capture line to show that nuclear reactions are indeed continuing into the third orbit.

The fluxes of the individual narrow nuclear lines relative to that of the 6.129 MeV ^{16}O line are listed in Table 1. These relative fluxes are averaged over fits to data obtained throughout the first orbit (3.64 – 4.08 UT) and during the first half of the second orbit where the statistics are adequate (4.67 – 5.11 UT). For the first orbit, fits to data obtained from off-pointed detectors during the early part (3.64 – 3.90 UT) are used and, to maximize the statistical significance, Sun-pointed detector data are used during the last 10 minutes (3.90 – 4.08 UT; see §3.1). For the second orbit, fits to data obtained from Sun-pointed detectors are used. The relative line fluxes derived from Sun- and off-pointed detector data during the last 10 minutes of the first orbit are in reasonable agreement, with the largest discrepancy being $<$2.5 σ. Also shown in the table are the average relative line fluxes derived by Share and Murphy (1995) for the 19 *SMM*/GRS flares. For γ-ray lines below 2 MeV, the June 4 relative fluxes are very similar to the *SMM*/GRS averages. The June 4 4.44 MeV ^{12}C flux, however, appears to be significantly higher than the *SMM*/GRS flux (by 5 σ); the implication of this is discussed further in §5.1.

We also note that the relative flux of the $\sim$7 MeV line complex from ^{16}O is significantly higher than the 19-flare average of the *SMM*/GRS analysis in which little flare-to-flare variation of this ratio was measured. We investigated whether this high flux ratio could be due to inadequacies of our assumed γ-ray model or to contamination of the line from spacecraft sources. The slight excess of count rate over the best-fit model (see Panel b of Figure 4) suggests that the model photon spectrum may be inadequate at these energies. We refit the data replacing the power law with either a broken power law or the sum of two power laws and found that the quality of fit was not significantly improved and the fitted line flux was unchanged. Contamination of the $\sim$7 MeV line could be due to γ-rays from capture of solar-flare neutrons by spacecraft iron or by iodine in the OSSE detector. The fact that the line flux appears to peak late in the first orbit when the neutrons are arriving lends support to this possibility. In their analysis of the June 4 flare, Bertsch *et al.* (1997) required a feature at $\sim$7.6 MeV from neutron capture on iron after the peak. However, if there were significant contamination, the derived flux of the $\sim$7 MeV line from off-pointed data would be significantly larger than that from Sun-pointed data because the detector

response to such sources is essentially the same for both detector orientations. Because the derived fluxes from the two orientations were consistent, we see no reason to doubt our measurement of this line. The implications of this high flux is discussed in §5.1. In the analysis that follows, the line is included in the sum of line fluxes from high-FIP elements. We have also performed the analysis without the line and found the results unchanged, indicating that our conclusions are not strongly dependent on this line.

4.1.2. Ambient Abundance Estimates

Because the emission of a given narrow γ-ray line is mostly dominated by the contribution from a single element, information about ambient elemental abundances can be obtained by comparing narrow-line fluxes. For comparison with the *SMM*/GRS analysis of Share and Murphy (1995), we have separately summed the fluxes of the >1 MeV lines from low-FIP elements Mg, Si and Fe (1.369, 1.778 and 1.238 MeV) and those of lines from high-FIP elements C, O and Ne (4.44, 6.129, 6.99 and 1.634 MeV). Averaged over the two-orbit data as above, the OSSE low FIP-to-high FIP ratio is 0.41 ± 0.02. This ratio is plotted in Figure 7 (open circle) along with the ratios for the 19 *SMM*/GRS flares (Share 1996, private communication). The horizontal line represents the weighted mean of this ratio (0.39) for the 19 flares and the value for June 4 is seen to be near this flare average. We note the excellent statistical significance of the June 4 result. If the ratio determined by Murphy *et al.* (1991) for the 1981 April 27 flare (flare number 2) represents a factor of three enhancement of the low-FIP/high-FIP abundance ratio over the photospheric value as they suggested, then the ratio determined here for the June 4 flare represents about a factor of 2.5 enhancement.

Share and Murphy (1995) have shown that the low FIP-to-high FIP line flux ratio varies significantly from flare to flare. The improved statistics available with the OSSE detectors allows us to search for variability of this ratio within a flare. Using Sun-pointed results for the second orbit and the last 10 minutes of the first orbit and off-pointed results for the rest of the first orbit, the probability that the derived ratios are consistent with their weighted mean is $< 10^{-4}$. The average ratios for each of the two orbits are 0.30 ± 0.03 and 0.57 ± 0.04 which differ by 5.6 σ. We conclude that the data suggest the low FIP-to-high FIP line flux ratio increased as the flare progressed. These values are also plotted in Figure 7 (filled circles) for comparison with the *SMM*/GRS results.

To show the time dependence of this ratio, the 2-minute data were rebinned into larger accumulation intervals ranging from ~6 to ~10 minutes to improve the statistical significance. The start and stop times of these intervals are 3.64 – 3.74, 3.74 – 3.90, 3.90 –

4.08, 4.67 – 4.82, 4.82 – 4.97 and 4.97 – 5.11 UT. Figure 6 displays these intervals on the >1 MeV narrow line time profile where the filled diamonds are from off-pointed detector data and the open diamonds are from Sun-pointed detector data. We note that the first interval essentially covers the emission peak and that the off- and Sun-pointed data during last 10 minutes of the first orbit give consistent results. Only data through the first half of the second orbit where the statistics are still adequate have been used. The time dependence of the low FIP-to-high FIP line flux ratio for the two orbits rebinned into these larger intervals is shown in Figure 8 along with a best-fit straight line fit to the Sun-pointed data only. This line has a positive slope with a significance of 5.2 σ. The probability that the data are randomly-distributed about this line is 0.17.

Since the low-FIP lines are concentrated in the 1 – 2 MeV region and the high-FIP lines are mostly in the 4 – 7 MeV region, we tested whether the observed variation of this ratio could be an artifact of an energy-dependent data problem. The comparison was repeated but for the ratio of the sum of >1 MeV low-FIP lines to the high-FIP 1.634 MeV Ne line alone so that all lines are now concentrated in the same energy range. The time profile of this ratio is plotted in Figure 9 and shows the same qualitative behavior as the low FIP to high FIP ratio. While the poorer statistics have reduced the significance of the difference of the two orbital values to 3.2 σ, the trend with time suggests that this low FIP-high FIP variability is not due to fitting problems.

4.2. The Broad-Line Component

The ratio of the flux in broad lines to the flux in narrow-lines gives a measure of the relative abundance of accelerated heavy particles to accelerated protons. However, because the broad-line component also contains emission from unresolved narrow lines produced by protons (see discussion in §3.3), any measured variation should represent a lower limit to the actual variation. Using Sun-pointed >0.1 MeV data only, the ratio of the >1 MeV flux in the *broad-line template* to the >1 MeV flux in narrow-lines averaged over the last 10 minutes of the first orbit and the first half of the second orbit is 2.83 $\pm$ 0.07. Using the same *broad line template*, the 19-flare *SMM*/GRS analysis (Share 1996, private communication) showed considerable flare-to-flare variation of this ratio, ranging from $\sim$2 to $\sim$7 with a weighted mean of 3.2 $\pm$ 0.2. The averages from each of the two June 4 orbits are 3.40 $\pm$ 0.12 and 2.19 $\pm$ 0.09. These values differ by 8.1 σ; the probability that the derived ratios are consistent with their weighted mean is $< 10^{-5}$. This suggests that the accelerated heavy ion to proton ratio decreased as the flare progressed.

4.3. Accelerated Proton Spectrum

In this section the spectral shape and energy content of the accelerated protons are derived from the measured γ-ray line fluxes. Flux ratios of lines whose production cross sections have different energy dependencies are sensitive to the proton spectral index. Because the 6.129 and 1.634 MeV de-excitation lines of O and Ne are relatively strong and their energy-dependent cross sections are distinctly different, their ratio is particularly useful for measuring the spectral hardness of interacting 5 – 20 MeV protons (Share and Murphy 1995; Ramaty *et al.* 1996). Because both lines are prompt, this ratio gives an *instantaneous* measure. Alternatively, because the neutrons producing the 2.223 MeV capture line are produced by higher-energy (30 – 100 MeV nucleon^{-1}) particles than those producing the de-excitation lines, the flux ratio of the neutron-capture line and a de-excitation line provides spectral information about 10 – 100 MeV protons (e.g., Ramaty *et al.* 1993). But because the neutron capture line is delayed relative to the de-excitation lines, the technique can only be properly used with flare-integrated data to provide an average index for the whole flare.

Assuming a power law form for the proton spectrum, the measured O/Ne flux ratios were converted to proton power law spectral indexes by using the thick target γ-ray line calculations of Ramaty *et al.* (1996; see their Figure 1) for Ne/O = 0.25 and two assumptions for the α/proton ratio of 0.1 and 0.5. The average index over both orbits was 4.0 $\pm$ 0.2 for α/proton = 0.1 and 4.4 $\pm$ 0.3 for α/proton = 0.5.

For the alternative technique, the fluence ratio of the neutron-capture line and the 4.44 MeV ^{12}C de-excitation line was used. The total fluences in these two lines from the June 4 flare, after linearly interpolating over gaps in the data due to earth occultation and applying a correction for saturation effects at the peak of the flare (see §3.3), are 1050 $\pm$ 19 and 189 $\pm$ 9 photons cm^{-2}, respectively. The OSSE measurements can be compared with the EGRET/TASC observations (Bertsch *et al.* (1997) beginning 81 s after the peak of emission until the end of the first orbit (the TASC was saturated during the peak). During this time period, the EGRET/TASC measured 2.223 and 4.439 line fluences of 678 $\pm$ 24 and 66 $\pm$ 3 photons cm^{-2}, respectively. The OSSE fluences for the same time period are 644 $\pm$ 12 and 75 $\pm$ 4 photons cm^{-2}, respectively, in good agreement (see also §4.6). Using the calculations of thick-target nuclear line and neutron production by Ramaty *et al.* (1996) and the measured 2.223-to-4.44 MeV line fluence ratio (5.56 $\pm$ 0.28), we obtain a flare-averaged proton power law index of 3.7 $\pm$ 0.1 for an α/proton ratio of 0.1 and 4.2 $\pm$ 0.1 for α/proton = 0.5. Here we have assumed impulsive-flare abundances and a downward isotropic angular distribution for the accelerated ions (see Ramaty *et al.* 1996). (The impulsive-flare composition has significant enhancements of Ne, Mg, Si and Fe in addition

to ^{3}He/α = 1.)

The values of the proton index derived using the O/Ne line fluence ratio with either α/proton = 0.1 or 0.5 (4.0 $\pm$ 0.2 and 4.4 $\pm$ 0.3) are in reasonable agreement with the corresponding indexes obtained using the neutron-capture/^{12}C line fluence ratio (3.7 $\pm$ 0.1 and 4.2 $\pm$ 0.1), differing by 1.2 and 0.6 σ, respectively. We note the better agreement using α/proton = 0.5 (see also §4.5). We also note that an assumption of gradual-flare abundances for the accelerated ions (see Ramaty *et al.* 1996) gave indexes in poorer agreement (4.8 and 3 σ differences, respectively).

Using the average spectral index derived from the neutron capture to 4.44 MeV line ratio and the flux in the 4.44 MeV line, we can obtain the flare-averaged proton spectrum using recent calculations of thick-target 4.44 MeV ^{12}C γ-ray line yield (Ramaty 1997, private communication) for Ne/O = 0.25. We assume α/proton = 0.5 based on the better agreement of both the spectral indexes derived above and the α-α line-to-high FIP line ratio (see §4.5). We further assume that the proton spectrum is a power law extending down to 1 MeV with a flat extension to lower energies. This spectrum is then integrated to obtain the number of accelerated protons and their energy content. After corrections for gaps in the data and saturation, the total number of protons with energy >30 MeV accelerated in the flare was (6.7 $\pm$ 1.2) $\times$ 10^{32} and the total energy contained in accelerated protons of all energies was (1.7 $\pm$ 0.2) $\times$ 10^{32} ergs. If we assume impulsive-flare abundances (see Ramaty *et al.* 1996), identical energy dependence for all ion spectra, and α/proton = 0.5, the total energy contained in accelerated ions was (1.0 $\pm$ 0.1) $\times$ 10^{33} ergs.

The time dependence of the proton spectral index derived from the measured O/Ne line flux ratios and calculated for α/proton = 0.5 is shown in Figure 10 where the 2-minute data have been rebinned as discussed in §4.1.2. These values are consistent (40% confidence) with a statistical distribution about their mean. The average indexes derived for the two orbits are 4.4 $\pm$ 0.3 and 4.3 $\pm$ 0.2, respectively, which differ by 0.3σ indicating that there is no significant evidence for spectral evolution of the accelerated proton spectrum. The same conclusion is reached for α/proton = 0.1. The time dependence of the instantaneous power in accelerated protons, $\dot{W}_p$, is shown in Figure 11.

4.4. Accelerated Electron Spectrum

4.4.1. Spectrum and Energy Content

An unambiguous measurement of the electron bremsstrahlung spectrum can be obtained using fits to >0.1 MeV data from Sun-pointed detectors after the peak of emission.

Assuming a power law form for the bremsstrahlung component, we derive an average index of 2.74 $\pm$ 0.01. The index was essentially constant, varying from its average value by less than 0.07 over the two-orbits of Sun-pointed data. This implies a similar constancy of the >0.1 MeV electron spectrum. Fits to off-pointed data during the peak of emission cannot be used to directly determine the bremsstrahlung spectrum because the bremsstrahlung cannot be easily distinguished from the broad-line component at energies >1 MeV. However, the bremsstrahlung flux during these times can be estimated from the difference between the total flux and the nuclear flux. The narrow lines and the 2.223 MeV neutron-capture line are well-measured with off-pointed data but the broad component is not. Using Sun-pointed data during the last 10 minutes of the first orbit (see §4.2) we found a broad-to-narrow ratio of 3.4. To estimate the bremsstrahlung flux we assume this ratio to be constant at this value throughout the orbit but we allow a large uncertainty as discussed below.

Shown in Figure 12 (filled diamonds) is the >1 MeV bremsstrahlung flux estimated from off-pointed detector data obtained during the first orbit. The uncertainties shown represent the range of flux values obtained by assuming broad-to-narrow ratios ranging from 2 to 7, the variation found in the 19-flare *SMM*/GRS analysis (see §4.2). We note that, after the peak of the June 4 flare, the ratio is probably not larger than 5 since larger assumed ratios resulted in significant over-subtraction and negative bremsstrahlung fluxes. Also shown in the Figure (open diamonds) are the measured >1 MeV bremsstrahlung fluxes directly obtained from Sun-pointed detector data from the first and second orbit. During the last 10 minutes of the first orbit, the Sun- and off-pointed bremsstrahlung are consistent.

We derive the corresponding accelerated electron spectrum from the measured bremsstrahlung using calculations of thick target bremsstrahlung production from power law electron spectra (Ramaty *et al.* 1993). The electron spectrum can then be integrated to obtain the total energy contained in the accelerated electrons. The total energy contained in electrons >0.1 MeV accelerated in the June 4 flare is estimated to be (1.7 $\pm$ 0.1) $\times$ 10^{31} ergs. The time profile of the instantaneous power in accelerated electrons >0.1 MeV in the interaction region, $\dot{W}_e$, is plotted in Figure 13. The uncertainties associated with the off-pointed detector measurements during the first orbit reflect the uncertainty in the broad-to-narrow ratio. The effects of allowing for a different bremsstrahlung spectrum during the peak of the flare are discussed in §5.2.2 and §5.2.3.

4.4.2. Comparison of Bremsstrahlung with Other Emissions

The derived high-time resolution >1 MeV bremsstrahlung flux is shown in Panel (a) of Figure 14 (filled diamonds) for the impulsive phase of the first orbit along with other emissions. The data have been rebinned into slightly longer time intervals to improve the statistical significance. Also shown in Panel (a) is the time profile of the 1-s 80 GHz radio data (thin curve) obtained with radiometers at the Nobeyama Radio Observatory, Japan (Ramaty *et al.* 1994; Enome 1995, private communication). Such gyrosynchrotron emission is produced predominantly by electrons of energies above 1 MeV, essentially the same electron energies that produce the >1 MeV bremsstrahlung. The radio data have been renormalized to the bremsstrahlung flux on the rising and falling portion of the primary peak. The three periods of enhanced emission are seen in both profiles. The early radio emission before each of the three γ-ray peaks may be due to gyrosynchrotron emission of electrons trapped in the corona where the matter density is too low for efficient γ-ray production (Ramaty *et al.* 1994). Their subsequent release into denser regions produced the γ-ray emission (see §5.2.4). We also note the lag in the maxima of the OSSE rates relative to the 80 GHz rate. Also shown in Panel (a) of Figure 14 is the time profile of the high-FIP line fluxes (multiplied by a factor of 300 for clarity) providing the interaction rate of 5 – 30 MeV protons. The proton interactions do not show a peak as intense as that of the electrons and they decay at a slower rate (see also §5.2.3).

In Panel (b) of Figure 14 we compare high temporal resolution profiles of the OSSE >1 MeV bremsstrahlung flux (filled diamonds), the OSSE background-subtracted >16 MeV γ-ray flux (open diamonds; DelSignore 1995), the 1-s 80-GHz radio data (thin curve), and the 1-s average count rate from the four Sun-facing BATSE CPDs (dotted curve). The CPD and 80 GHz data have been renormalized to the bremsstrahlung flux on the rising and falling portion of the primary peak. The >16 MeV flux has been renormalized to have the same peak flux as the bremsstrahlung. We again note the lag in the maxima of the OSSE and also BATSE CPD rate relative to the 80 GHz rate. We also note that the BATSE CPD count rate is due not only to electron bremsstrahlung but also nuclear emissions (see §5.2.4).

Since the proton power law spectral index derived for this flare (3.7 – 4.2) is too soft to produce a significant number of pions, the >16 MeV radiation must be bremsstrahlung from high-energy electrons. The comparison of the >1 MeV bremsstrahlung with the >16 MeV emission shows that the high-energy emission decayed more quickly, suggesting that the spectrum of accelerated electrons either softened after the peak or exhibited a transient high-energy tail at the peak. This is to be compared with the constancy found in the steepness of the 0.1 – ∼1 MeV electron spectrum measured later in the flare. Because

lower-energy electrons lose energy via collisions more rapidly than higher-energy electrons, a softening spectrum would argue against trapping of impulsively accelerated electrons in the corona, as assumed by Ramaty *et al.* (1994) in their analysis of the June 4 flare. However, if the magnetic field in coronal portion of the loop is sufficiently high, synchrotron losses could explain the rapid removal of the higher-energy electrons (see §5.2.4 for further discussion).

4.5. Accelerated α/Proton Ratio

An estimate of the accelerated α/proton ratio can be obtained by comparing the flux of the $\sim$0.45 MeV α–α line complex with that of narrow de-excitation lines. Since He is a high FIP element, the comparison is best made with lines from high-FIP elements. Using fits to Sun-pointed data, no evidence for variation of the α-α-to-high FIP line flux ratio with time was found, with an average value of 0.66 $\pm$ 0.04. Share and Murphy (1997a) measured this ratio for the 19 *SMM*/GRS flares and found no evidence of flare-to-flare variation, with a weighted average ratio of 0.49 $\pm$ 0.05.

We compare the measured June 4 α-α-to-high FIP ratio with predicted ratios determined for α/proton ratios of 0.1 and 0.5 using calculations of thick-target γ-ray line production (e.g., Ramaty, Kozlovsky and Lingenfelter 1979; Kozlovsky *et al.* 1997; see also Figure 4 of Share and Murphy 1997a). The ratio is fairly insensitive to the assumed accelerated heavy ion composition but does depend on the spectral index of the accelerated protons and the ambient [He]/[CNO] abundance. We assume coronal values for these abundances (Reames 1995: [He]/[O] = 57). Using the spectral index derived for α/proton = 0.1 (3.7; see §4.3), the predicted flux ratio is 0.34 $\pm$ 0.01 which is not consistent with the measured value of 0.66 $\pm$ 0.04 (a difference of 8 σ). However, using the spectral index derived for α/proton = 0.5 (4.2; see §4.3), the predicted flux ratio is 0.55 $\pm$ 0.04 which is in better agreement with the observed value (a difference of 1.9 σ). We conclude that the accelerated α/proton ratio for the 1991 June 4 flare is larger than 0.1 and probably closer to 0.5. This conclusion is consistent with the detailed analysis of the 1981 April 27 flare by Murphy *et al.* (1991) and the analysis of 19 *SMM*/GRS flares by Share and Murphy (1997a).

4.6. Photospheric ^{3}He/H Abundance Ratio

The time profile of the 2.223 MeV neutron capture line can be used to determine the photospheric ^{3}He/H ratio. Because of the time required for neutrons to slow down

and be captured on ^{1}H, neutron-capture photons are produced about 100 seconds after the production of the neutrons. The competing capture reaction ^{3}He(n,p)^{3}H produces no radiation but affects the delay of the 2.223 MeV line emission. To make a precise determination of the ^{3}He abundance, detailed calculations of the capture-line time dependence as a function of both the ^{3}He abundance and observing angle for thick-target interactions of accelerated particles with various assumed energy spectra and angular distributions are necessary. This has been done for the 1982 June 3 *SMM*/GRS flare (Hua and Lingenfelter 1987). To analyze the OSSE data, a simplified, empirical approach adopted by Prince *et al.* (1983) in their analysis of the June 3 flare is used. The neutron capture-line flux from an instantaneous production of neutrons is assumed to fall exponentially in time with a time constant τ given by (eq. 2 of Prince *et al.* 1983)

$$\tau = [\tau_{\rm H}^{-1} + \tau_{\rm He}^{-1} + \tau_{\rm d}^{-1}]^{-1}$$

where $\tau_{\rm H}$ is the time constant for capture on H, $\tau_{\rm He}$ is the time constant for capture on ^{3}He, and $\tau_{\rm d}$ is the neutron decay time. $\tau_{\rm H} = 1.4 \times 10^{19}/n_{\rm H}$ (s) and $\tau_{\rm He} = 8.5 \times 10^{14}/(R\ n_{\rm H})$ (s) where $n_{\rm H}$ is the hydrogen number density (cm^{-3}) and R is the ^{3}He/H ratio. Prince *et al.* argue that $n_{\rm H}$ should be $\sim 1.3 \times 10^{17}$ cm^{-3} due to a "plateau" in the solar density distribution at the top of the photosphere. They also restrict their fits to the first 150 seconds after the flare peak, but because the June 4 flare is less impulsive than the June 3 flare, all data from just prior to the peak (3.68 hours UT) to the end of the first orbit are used in this analysis. (We also investigated shorter integration times.) To confirm our implementation of the technique, we repeated the Prince *et al.* analysis of the 1982 June 3 flare and obtained a time constant of 88 seconds as compared to their published value of 89 seconds.

Panel (a) of Figure 15 displays a high time resolution (8 s and greater) plot of the 2.223 MeV neutron-capture line flux for the first orbit. Also shown in the Figure are 2.223 MeV line fluxes obtained with the EGRET/TASC (Bertsch *et al.* 1997). The agreement with the OSSE fluxes is remarkably good, especially considering the intensity of the flare and also the corrections to the EGRET fluxes due to overlying material. The small excess of the EGRET fluxes over the OSSE fluxes near the end of the orbit may be due to 2.223 MeV photons produced in the *CGRO* hydrazine tanks by solar-flare neutrons that were reaching their peak intensity at that time (see Figure 1 and discussion). The OSSE detectors are adequately shielded against such background radiation.

We make the plausible assumption that the time history of the summed high-FIP line fluxes (shown in Panel (b) of Figure 15) mirrors the interaction time profile of the accelerated particles producing neutrons in the flare. Using this production time profile, the predicted time profile of the neutron capture line is compared to the data in Figure

16; the dotted envelope represents a $\pm 1\sigma$ uncertainty. The best fit is achieved with $\tau = 104 \pm 6$ s and $\chi^2 = 49.6$ (d.o.f. $= 54$) corresponding to a 64% probability that the data is randomly distributed about the fit. Using the above equation, however, this best-fit value for the time constant is too long to give a physical value for the ^{3}He/H ratio. We tested whether this could be due to a hardening of the accelerated particle spectrum at high energies as the flare progressed by introducing a time-dependent neutron-production efficiency into the calculations, but the value of τ was not reduced. We also tried separately fitting sub-intervals of the flare (see, e.g., Rank 1995) and found that, for the intervals near the peak where the statistics were sufficient to obtain meaningful results, τ was again not reduced.

Inspection of the above equation shows that R depends sensitively on the assumed value of the plateau density. Prince *et al.* argue that a conservative lower limit to this density is 1×10^{17} cm^{-3}. Using this value, we obtain a ^{3}He/H ratio of $(1.3 \pm 0.5) \times 10^{-5}$ and provide a 2-σ upper limit of 2.3×10^{-5}.

4.7. Extended Proton Interactions

For flares located away from the solar limb, the narrow 2.223 MeV neutron capture line is the most sensitive indicator for the presence of nuclear reactions resulting from accelerated ions. Because the June 4 flare occurred at a heliocentric angle of 75°, this line can be used to search for nuclear emission preceding and following the impulsive phase. Plotted in Figure 17 is the flux observed in the 2.223 MeV neutron-capture line covering three orbits of observations. The fluxes for the first orbit are derived from fits to >1 MeV data from off-pointed detectors. For the second and third orbits they are from fits to >0.1 MeV spectra from Sun-pointed detectors. Nuclear interactions and the resultant γ-ray emission are clearly seen to continue after the peak of emission through at least the second orbit; i.e., for 2 hr.

We note that the flux of the 2.223 MeV line at the beginning of the second orbit appears to be higher than a simple extrapolation from the end of the first orbit would imply (see Figure 17). The effect is not as apparent in the summed flux of narrow lines flux (see Figure 6). This suggests the possibility of a high-energy acceleration episode occurring during satellite night. Also plotted in Figure 17 is the 80 GHz Nobeyama microwave data (with arbitrary normalization) attributed to gyrosynchrotron emission from >1 MeV electrons. There is evidence in this latter emission for an outburst during satellite night at about 4.4 hr. Struminsky *et al.* (1994) have used the microwave and ground-based neutron-monitor data to argue for such an additional episode producing high-energy particles.

The flux in the 2.223 MeV line averaged over the third orbit is $(1.1 \pm 0.2) \times 10^{-3}$ photons cm^{-2} s^{-1}, indicating that nuclear interactions are occurring during this time. However, as discussed in §3.2, there is an additional uncertainty in our determination of absolute fluxes due to day-to-day residuals remaining after background subtraction. For the 2.223 MeV line, these residuals were at a level of about 1×10^{-3} photons cm^{-2} s^{-1} a few days after the flare; i.e., comparable to the measured third-orbit flux. Fortunately, we can use the standard OSSE background subtraction technique as an alternative to the predictive algorithm. The standard technique has the advantage that the background systematic is significantly smaller than that of the predictive algorithm, but the statistics are poorer since only one detector views the Sun at a given time rather than three.

We have used the standard technique with data from the two chopping detectors to search for evidence of nuclear reactions not only the during the third orbit but also during the ∼3-day period surrounding the June 4 flare. Plotted in Figure 18 is the line flux derived from orbit-averaged data during this time period. (The orbit containing the peak of the flare and the following orbit are off scale and are excluded from this analysis.) Also plotted in the Figure is the *GOES* 1 – 8 Å X-ray profile. The 2.223 MeV line flux during the third orbit is $(1.5 \pm 0.5) \times 10^{-3}$ photons cm^{-2} s^{-1}, consistent with the value derived using the predictive algorithm. We can now say with 99.7% confidence (3 σ) that nuclear interactions are occurring during the third orbit. But Figure 18 shows that this flux may only be part of a general excess of emission occurring for several orbits both before and after the flare. We have separately summed the data accumulated during the flare-associated interval indicated in Figure 18 and the data accumulated during the orbits outside of the interval. The fitted 2.223 MeV line flux during the flare-associated interval was $(1.0 \pm 0.2) \times 10^{-3}$ photons cm^{-2} s^{-1} while the flux outside of the interval was $(0.1 \pm 0.1) \times 10^{-3}$ photons cm^{-2} s^{-1}. This suggests that throughout the several hours before and after the impulsive flare there was a significant level of nuclear interactions.

5. DISCUSSION

Using spectral observations of the 1991 June 4 solar flare, we have obtained information about the ambient plasma at the flare site and the composition and spectra of the accelerated ions and electrons. The main results are: (1) the ratio of the ambient abundance of elements with low FIP to those with high FIP was similar to the mean ratio determined for 19 *SMM*/GRS flares and appears to have increased as the flare progressed; (2) a model-dependent 2-σ upper limit of 2.3×10^{-5} was obtained for the photospheric ^{3}He/H abundance ratio; (3) based on current models of γ-ray production, the accelerated α/proton ratio was significantly larger than 0.1 and probably close to 0.5 and the relative abundance

of the accelerated ions was probably more like the composition of impulsive-flares observed in interplanetary space rather than gradual-flares; (4) the accelerated heavy ion-to-proton ratio appears to have decreased as the flare progressed; (5) the high-energy ($\gtrsim$ 16 MeV) component of the accelerated electrons was more impulsive than the lower-energy ($\sim$MeV) component; (6) the ratio of electron bremsstrahlung to the flux in narrow γ-ray lines decreased as the flare progressed; (7) the total energy in accelerated ions exceeded the energy in >0.1 MeV electrons; (8) the derived magnetic field intensity in the coronal loop was probably larger than 200 G (based on a specific model); (9) the nuclear reactions producing the γ rays continued for more than 3 hours and resulted from ions that were probably accelerated continuously rather than impulsively followed by trapping; and (10) energetic ions may have been present for several hours prior to and following the impulsive phase of the flare. Each of these is discussed below.

5.1. Ambient Abundance Estimates and Temporal Variation

5.1.1. Ambient Abundances

The measured fluxes of nuclear γ-ray lines have been used to obtain information about the composition of the ambient flare plasma. The flare-averaged narrow nuclear de-excitation line fluxes relative to that of the 6.13 MeV ^{16}O line were mostly similar to the averages measured for the 19 *SMM*/GRS flares (Share and Murphy 1995; see Table 1) suggesting that the June 4 ambient abundances were similar to those of other γ-ray flares. However, we note that the relative flux of the 4.44 MeV ^{12}C line appears to be high compared to the *SMM*/GRS average, although there were *SMM*/GRS flares with relative fluxes consistent with the June 4 value. The June 4 measured flux ratio corresponds to an ambient C/O abundance ratio of 0.54 $\pm$ 0.04, obtained using calculations of thick-target γ-ray line production (e.g., see Figure 6 of Ramaty *et al.* 1996) and the flare-averaged accelerated proton spectral index of 4.3 (derived with an assumed accelerated α/proton ratio of 0.5). The result is independent of assumptions for the other ambient abundances and for the α/proton ratio. This derived C/O abundance ratio is high (2.2 σ) relative to the 19-flare *SMM*/GRS-flare average of 0.4 $\pm$ $\sim$0.05 derived by Ramaty *et al.* (1996); however, it is consistent (at >93% confidence level) with measurements of photospheric and coronal C/O abundance ratios ranging from 0.43 to 0.48 (see Anders and Grevesse 1989; Garrard and Stone 1993; Reames 1995; Grevesse and Noels 1993; Grevesse, Noels and Sauval 1996).

The relative flux of the $\sim$7 MeV line complex from ^{16}O is also significantly higher than the 19-flare average of the *SMM*/GRS analysis. We investigated whether this high flux

ratio could be due to inadequacies of our assumed γ-ray model or to contamination of the line from spacecraft sources but conclude that our measurement of this line is accurate. Calculations of thick-target γ-ray line production similar to those of Ramaty *et al.* (1996) show that the measured June 4 ratio can only be achieved with extreme values for both the accelerated proton spectral index (<2.5) and the accelerated α/proton ratio (>1). However, this hard index is inconsistent with the measured value for this flare and such a high α/proton ratio is unlikely. We have no satisfactory explanation for the high flux of the $\sim$7 MeV line.

The flare-averaged ratio of >1 MeV narrow-line fluxes from low-FIP elements to those from high-FIP elements for the June 4 flare is consistent with the mean ratio determined for 19 *SMM*/GRS flares (Share and Murphy 1995; Share 1996, private communication) where significant flare-to-flare variability was found. The June 4 ratio suggests that the ambient low-FIP elements at the interaction site are enhanced relative to high-FIP elements by about a factor of 2.5 compared to photospheric abundances.

The photospheric ^{3}He/H ratio is important for cosmological models, stellar evolution and implications of the solar ^{4}He/H ratio (Share and Murphy 1997b). Gamma-ray line measurements provide a measure of this ratio because the delayed time profile of the 2.223 MeV line from neutron capture on H is strongly affected by absorption on ^{3}He. Previous line measurements for the 1982 June 3 flare yielded ratios of $< 3.8 \times 10^{-5}$ (Prince *et al.* 1983) and $(1.2 - 2.3 \pm 1.2) \times 10^{-5}$ (Hua and Lingenfelter 1987). We have used the simplified approach of Prince *et al.* (1983) which models the neutron-capture line decay time with a simple exponential. Physical values could only be obtained if the average density at the neutron-capture site is as small as 1×10^{17} H cm^{-3}. For this value, a 2-σ upper limit for the ^{3}He/H ratio is 2.3×10^{-5}, consistent with the values obtained for the 1982 June 3 flare by both Prince *et al.* and Hua and Lingenfelter. Detailed modeling as was done by Hua and Lingenfelter (1987) for the 1982 June 3 flare are required to provide a better estimate of this ratio.

5.1.2. Abundance Variations

Using *SMM*/GRS data, Share and Murphy (1995) found significant variations of the low FIP-to-high FIP line ratio from flare to flare. With the improved statistics available with the OSSE detectors, we have searched for variability of this ratio within the June 4 flare. The flux ratios measured for the first and second orbits of emission were different (5.6 σ), increasing from more photospheric to more coronal values. The first-orbit ratio corresponds to about a factor of two enhancement of the low-FIP/high-FIP abundance

ratio relative to the photosphere and the second-orbit ratio to about a factor of 3.5, or what is observed in the corona. Such variability could possibly be due to time-dependent compositional changes at the flare site, but the time scale is probably too short for this to be a reasonable explanation. Alternatively, the location of the γ-ray production site could have changed with time, progressing from deeper in the chromosphere-photosphere toward the corona. This could happen if the height of the magnetic field mirroring point increased as the flare progressed. If this is the case, γ-ray measurements can be used to map the structure of the solar atmosphere during flares.

5.2. Accelerated Particle Spectra, Composition and Energy Content

5.2.1. Accelerated Protons and Ions

The spectrum of the accelerated protons can be studied using measurements of narrow γ-ray lines. For the June 4 flare, the instantaneous accelerated proton spectral index in the 5 – 30 MeV energy range was determined using the 6.129-to-1.634 MeV line (O/Ne) flux ratio. No significant evidence for spectral evolution of the accelerated proton spectrum was found, with flare-averaged indexes of 4.0 ± 0.2 and 4.4 ± 0.3 for α/proton ratios of 0.1 and 0.5, respectively. Using the alternative technique for determining a flare-averaged spectral index based on the ratio of the 2.223 MeV neutron-capture line and the 4.44 MeV ^{12}C de-excitation line, we found indexes of 3.7 ± 0.1 and 4.2 ± 0.1 for assumed α/proton ratios of 0.1 and 0.5, respectively. The assumption of α/proton = 0.5 provided better agreement between the two index-determining techniques (a difference in the indexes of 0.6 σ) than did α/proton = 0.1 (a difference of 1.2 σ). Ramaty *et al.* (1996) derived proton spectral indexes for the 19 *SMM*/GRS flares using the O/Ne line flux ratio. The indexes varied between 2 and 6 with a mean of $\sim$3.8 and $\sim$4.3 for α/proton = 0.1 or 0.5, respectively. The proton spectrum of the June 4 flare appears to be typical of γ-ray flares.

The power law indexes deduced here are softer than those we deduced earlier for this flare (Murphy *et al.* 1993a; $\simeq 2.8$) because (1) the additional data at the peak included here significantly increased the measured 4.439 MeV line fluence relative to the 2.223 MeV line fluence and (2) impulsive-flare accelerated-particle abundances are now used (see below).

The abundances of the accelerated particles and their variability can provide constraints on models of particle acceleration in solar flares (e.g., Temerin and Roth 1992; Miller and Vinas 1993; Miller and Roberts 1995). A measure of the accelerated α/proton ratio can be obtained by comparing the flux of the $\sim$0.45 MeV α–α line with the sum of line fluxes from high-FIP elements. The flare-averaged flux ratio of the α–α line to the high-FIP lines

was 0.66 ± 0.04. Using calculations of thick-target γ-ray line production, this measured value corresponds to an accelerated α/proton ratio larger than 0.1 and closer to 0.5 for an assumed ambient ^{4}He/H ratio of 0.1. In support of this conclusion, assuming α/proton = 0.5 yields a proton spectral index derived using the neutron capture-to-^{12}C line flux ratio that is in better agreement with the index derived using the O/Ne line flux ratio (see above). In their analysis of 19 *SMM*/GRS flares, Share and Murphy (1997a) also concluded that an α/proton ratio closer to 0.5 was required, consistent with the 1981 April 27 flare analysis of Murphy *et al.* (1991). No evidence for variation of the accelerated α/proton ratio with time during the June 4 flare was found.

The ratio of the flux in broad γ-ray lines to the flux in narrow lines gives an indication of the accelerated heavy ion-to-proton ratio. Because of difficulties fitting broad line features, the broad component was not fit with individual Gaussians. Instead, a *broad-line template* based on measurements of *SMM*/GRS spectra was used instead. The flare-averaged ratio of the flux in the *template* to the flux in narrow γ-ray lines >1 MeV (2.83 ± 0.07) was consistent with the mean obtained from the 19-flare *SMM*/GRS analysis where flare-to-flare variation of this flux ratio was measured. Using the OSSE data for the June 4 flare, we searched for variation of this ratio with time. The averages for the two orbits were found to be different (8.1 σ), suggesting that the accelerated heavy ion-to-proton ratio decreased as the flare progressed. As mentioned above, the accelerated α/proton ratio showed no significant evidence of temporal variation.

Using current models of γ-ray production, constraints can be placed on the relative abundances of heavy (i.e., $>^4$He) accelerated ions. To achieve agreement between the two proton spectral index-determining techniques required assuming impulsive-flare abundances (see Ramaty *et al.* 1996) for the accelerated particles. The alternative assumption of gradual-flare abundances did not provide agreement. This is consistent with the 1981 April 27 flare analysis of Murphy *et al.* (1991) and the 19 *SMM*/GRS flare analysis of Ramaty *et al.* (1996). In their analysis of the *GRANAT*/PHEBUS γ-ray data from the behind-the-limb flare on 1991 June 1, Ramaty *et al.* (1997) found that the composition of the accelerated particles producing the γ rays also showed heavy-element enhancements typical of impulsive flares. This impulsive-flare composition has ^{3}He/α = 1 in addition to significant enhancements of Ne, Mg, Si and Fe.

The number of accelerated protons and their energy content can be determined using the flare-averaged proton spectral index derived for α/proton = 0.5 (4.2 ± 0.1) and the flux in the 4.44 MeV ^{12}C line (189 ± 9 photons cm^{-2}). Assuming the spectrum is a power law extending down to 1 MeV with a flat extension to lower energies, the total number of protons with energy >30 MeV accelerated in the June 4 flare was (6.7 ± 1.2) × 10^{32}

and the total energy contained in protons of all energies was $(1.7 \pm 0.2) \times 10^{32}$ ergs. Ramaty *et al.* (1994) determined the number of protons accelerated in the June 4 flare to be 5.7×10^{32}. Assuming impulsive-flare abundances for the accelerated particles, identical energy dependence for all ion spectra, and α/proton = 0.5, the total energy contained in accelerated ions was $(1.0 \pm 0.1) \times 10^{33}$ ergs. This is larger than the largest energy contained in ions for any of the 19 *SMM*/GRS flares (Ramaty *et al.* 1995).

5.2.2. Accelerated Electrons

At times after the peak of emission, the electron bremsstrahlung spectrum can be directly measured with Sun-pointed detector data. No evidence for temporal evolution of the spectral index was found; it varied from its average value of 2.74 by less than 0.07. This spectral index corresponds to a power law index of ~3.9 for the accelerated electrons. The bremsstrahlung indexes measured for 84 strong *SMM*/GRS flares (Vestrand *et al.* 1997) varied between 2 and 6 with a mean of 2.86 for flares occurring at heliocentric angles greater than 60° (the June 4 flare occurred at 74.5°). The June 4 accelerated electron spectrum appears to be typical of γ-ray producing flares.

During the peak of the flare, the electron bremsstrahlung cannot be directly measured with the >1 MeV data from off-pointed detectors. The bremsstrahlung component was estimated by subtracting the flux due to nuclear emissions (assuming a constant ratio for the broad-to-narrow line fluxes) from the total observed flux. The total energy contained in electrons >0.1 MeV can be estimated by assuming the electron spectral index to be constant during the peak at the average value (2.74) directly measured later in the flare. If the June 4 flare is similar to most observed γ-ray flares, then the spectrum would be expected to be harder during the peak than during the decay (Dennis 1988). The comparison of the estimated >1 MeV bremsstrahlung with the >16 MeV flux at the peak may, in fact, indicate a softening of the spectrum with time. This >16 MeV emission (which is probably also bremsstrahlung but from high-energy electrons) was much more impulsive and decayed much more rapidly, suggesting that the accelerated electron spectrum during the peak softened over a broad energy range (or exhibited a transient high-energy tail). This suggests that our energy estimate at the peak determined using the index measured during the decay phase is an upper limit to the actual value. Our estimate for the total energy contained in electrons >0.1 MeV accelerated in the June 4 flare is $(1.0 \pm 0.1) \times 10^{31}$ ergs.

However, if the spectrum during the peak were indeed steeper, in contrast to our argument above, the derived energy in electrons would be higher. We can obtain a conservative upper limit to the total energy in >0.1 MeV electrons based on the total

energy in >0.02 MeV electrons measured with Ulysses (Kane *et al.* 1995). We note that the Ulysses value itself may represent an upper limit to the >0.02 MeV non-thermal electron energy since the time profile of the >0.025 MeV count rate (shown in Panel (a) of Figure 14; Kane *et al.* 1997) is much more gradual than the OSSE bremsstrahlung and is therefore suggestive of thermal origin. Kane *et al.* (1995) do not give the total energy of the electrons for the June 4 flare but only the energy deposition *rate* at the peak (2.5×10^{31} ergs s^{-1}). From the OSSE measurements, the estimated instantaneous power in >0.1 MeV electrons at the peak of the flare was $(1.6 \pm 0.1) \times 10^{29}$ ergs s^{-1}. If the electron spectrum is assumed to extend to lower energies as an unbroken power law with an index of 2.74, the >0.02 MeV electron energy deposition rate from the OSSE measurements would be $(2.8 \pm 0.2) \times 10^{30}$ ergs s^{-1}, or about an order of magnitude lower than the Ulysses measurements. This difference suggests that either the electron spectrum steepens below 0.1 MeV thermal emission is contaminating the Ulysses measurement. We scale our estimated energy in >0.1 MeV electrons by this factor of ten to obtain a conservative upper limit of 1×10^{32} ergs.

5.2.3. Energetics of Accelerated Ions and Electrons

A fundamental question of particle acceleration concerns the relative efficiency of electron and proton acceleration. The estimated total energy in >0.1 MeV electrons derived from the OSSE data was $(1.0 \pm 0.1) \times 10^{31}$ ergs while the total energy in protons was $(1.7 \pm 0.2) \times 10^{32}$ ergs. For this flare, the total energy in accelerated protons exceeded the energy in accelerated >0.1 MeV electrons by an order of magnitude (see Emslie 1983; Emslie *et al.* 1996). The energetic importance of ions was has been emphasized by Simnett (1995; see also Ramaty *et al.* 1995 and Mandzhavidze and Ramaty 1996). Assuming impulsive-flare accelerated-particle abundances and α/proton = 0.5, the total energy of all ions would be another factor of 6 higher than that of just the protons. We note that the conservative upper limit for the total energy in >0.1 MeV electrons, 1×10^{32} ergs, is still less than that of the protons and an order of magnitude less than that of ions assuming impulsive-flare abundances.

The above estimate of proton energy is based on a power-law spectrum extending down to a "cut-off" energy of 1 MeV with a flat extension to lower energies. If the cut-off energy were higher, the energy in accelerated protons could be less. We have used calculations of γ-ray line production to explore the dependence of the derived proton spectrum on cut-off energy. As the cut-off energy is increased, the required proton spectrum derived from the O/Ne line flux ratio steepens because of the low threshold energy of Ne excitation. But the cut-off energy cannot be larger than about 2 MeV; otherwise, the spectral index derived using the O/Ne ratio becomes inconsistent with the index derived using the

neutron-capture/^{12}C line flux ratio. A cut-off energy of 2 MeV rather than 1 MeV reduces the energy in the protons by less than a factor of 4. We conclude that the acceleration process in flares is thus capable of producing particles that are energetically dominated by ions, as in the June 4 flare, or by electrons, as in electron-dominated episodes of some flares (see Rieger and Marschhauser 1990).

Note that while the energy in accelerated ions may be greater than that in electrons, the flux in nuclear γ-ray lines relative to the flux in bremsstrahlung is not. This is because the efficiency for γ-ray production by protons via nuclear excitation is less than that by electrons via bremsstrahlung. During the peak of the flare, the bremsstrahlung flux accounted for 40% to 85% of the total >1 MeV flux, depending on the assumed broad-to-narrow line flux ratio. As the flare progressed, the bremsstrahlung/nuclear-line ratio decreased (the probability that the data are consistent with a constant is 6×10^{-4}), suggesting a corresponding decrease in the accelerated electron-to-proton ratio. The bremsstrahlung/nuclear-line ratio is shown in Figure 19.

5.2.4. Electron Trapping Time and the Coronal Magnetic Field

Ramaty *et al.* (1994) derived estimates of the magnetic field in coronal loops from electron trapping times. The trapping times were derived based on a model in which electrons spiral in a flare loop emitting gyrosynchrotron radiation and, after a mean time τ, escape down the loop to higher densities where they emit bremsstrahlung. Ramaty *et al.* used the BATSE CPD rate as a monitor of the bremsstrahlung. Based on a comparison of this rate with the 80 GHz emission, they concluded that the magnetic field in the loop was larger than 100 G.

We have used complementary OSSE spectral measurements of the flare to obtain a revised estimate of the magnetic field. OSSE has provided improved measurements for two relevant parameters: (1) the BATSE CPD instrument response appears to be a factor of $\sim$2.5 low and (2) about 85% of the BATSE CPD rate at the peak of the flare may be due to bremsstrahlung, in contrast to the 100% originally assumed. Combining these OSSE measurements yields an absolute reduction in the bremsstrahlung-to-radio emission ratio of 2.5 / 0.85 = 2.9. This yields revised trapping times based on Table 3 of Ramaty *et al.* (1994) which are presented in our Table 2 for various electron spectral indexes and magnetic field intensities.

Ramaty *et al.* (1994) estimated a value of 10 s for the bremsstrahlung decay time based on the decay of the BATSE CPD rate. Table 2 shows that to achieve trapping times $\lesssim 10$ s with $s_e \simeq 4$ requires a magnetic field $\gtrsim 300$ G. If the decay time of the bremsstrahlung is

longer than 10 s, as may be indicated by the OSSE-derived bremsstrahlung (see Panel (b) of Figure 14), then the required magnetic field could be reduced but would probably still be larger than 200 G. Such high magnetic fields may be required to explain the rapid depletion of the >16 MeV electrons; as discussed in §4.4.2, under the trapping scenario the electron spectrum should harden with time, but the OSSE >16 MeV observations show that the high-energy bremsstrahlung decays faster than the ∼1 MeV bremsstrahlung (also see the discussion of the next section).

5.3. Extended Accelerated-Particle Interactions

The mean duration of γ-ray flares observed by *SMM*/GRS was about 7 min, with the longest lasting about 1 hr. More recent measurements have shown that γ-ray flares can last for several hours, with the 1991 June 11 flare lasting up to 8 hours (Kanbach *et al.* 1993). Using the 2.223 MeV neutron-capture line as an indicator of proton interactions, we found that nuclear reactions associated with the impulsive flare continued through the second orbit; i.e., for at least two hours after the peak of emission. This raises the following question: Did these reactions result from particles that were accelerated early in the flare and were trapped or did they result from particles that were continuously accelerated? Because lower-energy particles lose energy more quickly than higher-energy particles, an indication of trapping would be a continuously-hardening proton spectrum (Mandzhavidze and Ramaty 1996). Direct measurement of the proton spectral index using the O/Ne line flux ratio indicates that the spectral index did not change with time, although the uncertainties are large enough to allow for a hardening of at least a full index. A comparison of the time profiles of the summed flux of lines from high-FIP elements and the 2.223 MeV neutron-capture line (shifted back in time ∼100 seconds to account for its delay) also shows no indication of a hardening proton spectrum which would reveal itself in a continuously increasing neutron-capture to high-FIP line ratio (compare Figures 6 and 17). Both of these emissions decay with nearly identical time constants. We conclude that the long-lasting nuclear γ-ray emission of the June 4 flare was probably due to continued ion acceleration rather than trapping. Using COMPTEL data, Rank *et al.* (1996; 1997) obtained a similar comclusion for the extended emission phases of the 1991 June 9, 11 and 15 flares.

The evidence for continued acceleration of electrons is less compelling. Under a trapping scenario, electron bremsstrahlung would be expected to decay faster than nuclear line emission because electrons lose energy faster than protons (Ramaty and Mandzhavidze 1994). This appears to be the case for the June 4 flare (see §5.2.3 and Figures 14 and 19) and so is suggestive of trapping. However, while a more rapid decay is a necessary consequence of trapping, it is not sufficient to prove trapping. The electrons could be accelerated

continuously with a decrease in the efficiency of electron acceleration relative to proton acceleration explaining the more rapid bremsstrahlung decay. Indeed, an argument in favor of continuous electron acceleration is the fact that the high-energy (>16 MeV) electrons decay more rapidly with time than the ~MeV electrons, at least over the short time scales associated with the peak of emission (see §4.4.2). This implies a softening spectrum while the spectrum of trapped electrons should harden. We note, however, that the assumption of trapped electrons has been made by Ramaty *et al.* (1994) in their analysis of the peak of the June 4 flare and has provided consistency between the 80 GHz radiation and the ~MeV γ-rays. We have also made this assuption in §5.2.4 where we repeated the Ramaty *et al.* (1994) analysis using the revised flare parameters obtained with the OSSE data. We have suggested that if these impulsive electrons are trapped, the more rapid decay of the >16 MeV electrons relative to the ~MeV electrons might be due to gyrosynchrotron losses. Even if the longer-term bremsstrahlung were due to continuously-accelerated electrons, the shorter-term impulsive electrons could be associated with a separate magnetic loop more conducive to trapping.

We searched for 2.223 MeV line emission at times other than the impulsive phase of the flare. Evidence for low-level emission was found during the several orbits prior to and following the flare orbits (see Figure 18) at an average flux of $(1.0 \pm 0.2) \times 10^{-3}$ photons cm^{-2} s^{-1}. This extended emission implies the existence of energetic ions at times other than those directly associated with the impulsive phase for up to 18 hr surrounding the flare. Such emission could be due to a number of microflares occurring during this period; a *GOES* M1.5 flare at about day 154.9 is visible in Figure 18. We note, however, that a larger M4.8 flare occurred at about day 156.1 without any increase in γ rays. Alternatively, the γ-ray emission could be due to long-term trapping of energetic particles in the corona (e.g., the model of Elliot 1964).

Simnett *et al.* (1986) searched for pre-flare emission in 8 flares observed by the *SMM*/GRS using the 4.44 MeV ^{12}C line but found no evidence for emission above their sensitivity threshold ($\sim 1 \times 10^{-3}$ photons cm^{-2} s^{-1}) at the 2-σ level. Rieger (1994) reported bursts of γ-ray emission on the rising portion of three *SMM*/GRS flares but concluded that the emission was most probably electron bremsstrahlung. In their analysis of several years of *SMM*/GRS data, Harris *et al.* (1992) obtained a 3-σ upper limit of 8.6 $\times 10^{-5}$ photons cm^{-2} s^{-1} for the 2.223 MeV line flux during periods of high solar activity excluding the times of flares (1.3×10^7 s livetime). It is important to observe flares in Cycle 23 with instruments as sensitive as OSSE to determine if this extended emission is characteristic of flares.

We wish to acknowledge Kellie McNaron-Brown, William Purcell, Byron Leas and

Daniel Messina for their help in analyzing the OSSE data. This work was supported by NASA DPR S-10987-C, NASA DPR S-92556-F and the Office of Naval Research.

REFERENCES

Anders, E., & Grevesse, N. 1989, Geochim. et Cosmochim. Acta, 53, 197

Barat, C., Trottet, G., Vilmer, N., Dezalay, J.-P., Talon, R., Sunyaev, R., Terekhov, O., & Kuznetsov, A. 1994, ApJ, 425 L109

Bertsch, D. L., Dingus, D. L., Esposito, J. A., Fichtel, C. E., Hartman, R. C., Hunter, S. D., Kanbach, G., Kniffen, D. A., Lin, Y. C., Mattox, J. R., Mayer-Hasselwander, H. A., Michelson, P. F., von Montigny, C., Mukherjee, R., Nolan, P. L., Schneid, E., Sreekumar, P., & Thompson, D. J. 1997, ApJ, submitted

Chiba, N., Dion, G. M., Hayashida, N., Honda K., Honda, M., Inuie, N., Kadota, K., Kakimoto, F., Kamata, K., Kawaguchi, S., Kawasumi, N., Matsubara, Y., Nagano, M., Ohoka, H., Teshima, M., Tsushima, I., Yoshida, S., Yoshii, H., & Yoshikoshi, T. 1992, Astroparticle Phys., 1, 27

Chupp, E. L. 1987, Phys. Scripta, T18, 5

DelSignore, K. W. 1995, Ph.D. thesis, Case Western Reserve University

Dennis, B. R. 1988, Sol. Phys., 118, 49

Elliot, H. 1964, Planetary Sp. Sci., 12, 657

Emslie, A. G. 1983, Sol. Phys., 84, 263

Emslie, A. G., Henoux, J.-C., Mariska, J. T., & Newton, E. K 1996, ApJ, 470, L131

Enome, S. 1995, private communication

Garrard, T. L., & Stone, E. C. 1993, 23rd Internat. Cosmic-Ray Conf. (Calgary), 3, 384

Grevesse, N., & Noels, A. 1993, in Origin and Evolution of the Elements, ed. N. Prantzos, E. Vangioni-Flam & M. Casse (Cambridge:University of Cambridge), 14

Grevesse, N., Noels, A. & Sauval, A. J. 1996, in Cosmic Abundances, ed. S. Holt & G. Sonneborn (San Francisco:Astronomical Society of the Pacific), 116

Gurnett, D. A., Kurth, W. S., Allendorf, S. C., & Poynter, R L. 1993, Science, 262, 199

Harris, M. J., Share, G. H., Beall, J. H., & Murphy, R. J 1992, Sol. Phys., 142, 171

Hua, X.-M., & Lingenfelter, R. E. 1987, ApJ, 319, 555

Hudson, H., & Ryan, J. 1995, ARA&A, 33, 239

Johnson, W. N., Kinzer, R. L., Kurfess, J. D., Strickman, S M., Purcell, W. R., Grabelsky, D. A., Ulmer, M. P., Hillas, D. A., Jung, G. V., & Cameron, R. A. 1993, ApJS, 86, 693

Kanbach, G., Bertsch, Fichtel, C. E., Hartman, R. C., Hunter, S. D., Kniffen, D. A., Kwok, P. W., Lin, Y. C., Mattox, J. R., Mayer-Hasselwander, H. A., Michelson, P. F., von Montigny, C., Nolan, P. L., Pinkau, K., Rothermel, H., Schneid, E., Sommer, M., Sreekumar, P., & Thompson, D. J. 1993, A&AS, 97, 349

Kane, S. R., Hurley, K. McTiernan, J. M., Sommer, M., Boer, M., & Niel, M. 1995, ApJ, 446, L47

Kane, S. R., Hurley, K., McTiernan, J. M., Boer, M., & Niel, M. 1997, in preparation

Kozlovsky, B. & Ramaty, R. 1974, ApJ, 191, L43

Kozlovsky, B. & Ramaty, R. 1977, Ap. Letters, 19, 19

Kozlovsky, B., Murphy, R. J., & Ramaty, R. 1997, in preparation

Lin, R. P., Schwartz, R. A., Pelling, R. A., & Hurley, K C. 1981, ApJ, 251, L109

Mandzhavidze, N., and Ramaty, R. 1996, abstract for the 188th Meeting of the AAS, AIP

Mandzhavidze, N., Ramaty, R., Bertsch, D. L., & Schneid, E J. 1996, in High Energy Solar Physics, ed. R. Ramaty, N. Mandzhavidze, & X.-M Hua (New York:Am. Inst. Phys.), 374, 225

McDonald, F. B., Keppler, E., & Reuss, M. K. 1995, Sp. Sci Rev., 72, 359

Miller, J. A., & Roberts, D. A. 1995, ApJ, 452, 912

Miller, J. A., & Vinas, A. F. 1993, ApJ, 412, 386

Muraki, Y., Murakami, K., Miyazaki M., Mitsui, K., Shibata, S., Sakakibara, S., Sakai, T., Takahashi, T., Yamada, T., & Yamaguchi, K. 1992, ApJ, 400, L75

Murphy, R. J., Hua, X.-M., Kozlovsky, B., & Ramaty, R 1990a, ApJ, 351, 299

Murphy, R. J., Kozlovsky, B., & Ramaty, R. 1988, ApJ, 331, 1029

Murphy, R. J., Ramaty, R., Kozlovsky, B., & Reames, D. V 1991, ApJ, 371, 793

Murphy, R. J., Share, G. H, Letaw, J. R., & Forrest, D. J 1990b, ApJ, 358, 298

Murphy, R. J., Share, G. H., Forrest, D. J., Grabelsky, D. A., Grove, J. E., Jensen, C. M., Johnson, W. N., Jung, G. V., Kinzer, R. L., Kroeger, R. A., Kurfess, J. D., Matz, S. M., Purcell, W. R., Strickman, M. S., Ulmer, M. P., & Vestrand, W. T. 1993a, 23rd Internat. Cosmic-Ray Conf. (Calgary), 3, 99

Murphy, R. J., Share, G. H., Forrest, D. J., Grabelsky, D. A., Grove, J. E., Jensen, C. M., Johnson, W. N., Jung, G. V., Kinzer, R. L., Kroeger, R. A., Kurfess, J. D., Matz,

S. M., Purcell, W. R., Strickman, M. S., Ulmer, M. P., & Vestrand, W. T. 1994, in High-Energy Solar Phenomena – A New Era of Spacecraft Measurement, Waterville Valley, NH, ed. J. Ryan & W Vestrand (New York:Am. Inst. Phys.), 294, 15

Murphy, R. J., Share, G. H., Grove, J. E., Johnson, W. N., Kinzer, R. L., Kroeger, R. A., Kurfess, J. D., & Strickman, M. S. 1993b, in Compton Gamma-Ray Observatory, St. Louis Mo., ed. M. Friedlander, N. Gehrels & D. Macomb (New York:Am. Inst. Phys.), 280, 619

Murphy, R. J., Share, Grove, J. E., Johnson, W. N., Kinzer, Kurfess, J. D., Strickman, & Jung, G. V. 1996, in High Energy Solar Physics, ed. R. Ramaty, N. Mandzhavidze, & X.-M. Hua (New York:Am. Inst. Phys.), 374, 184

Prince, T. A., Forrest, D. J., Chupp, E. L., Kanbach, G., & Share, G. H. 1983, 18th Internat. Cosmic-Ray Conf. (Bangalore), 4, 79

Ramaty, R., & Mandzhavidze, N. 1994, in High-Energy Solar Phenomena – A New Era of Spacecraft Measurement, Waterville Valley, NH, ed. J Ryan & W. Vestrand (New York:Am. Inst. Phys.), 294, 26

Ramaty, R. 1997, private communication

Ramaty, R., & Murphy, R. J. 1987, Sp. Sci. Rev., 45, 213

Ramaty, R., Kozlovsky, B., & Lingenfelter, R. E. 1975, Sp Sci. Rev., 18, 341

Ramaty, R., Kozlovsky, B., & Lingenfelter, R. E. 1979, ApJS, 40, 487

Ramaty, R., Mandzhavidze, N., Barat, C. & Trottet, G 1997, ApJ, 479, 458

Ramaty, R., Mandzhavidze, N., & Kozlovsky, B., 1996, in High Energy Solar Physics, ed. R. Ramaty, N. Mandzhavidze, & X.-M. Hua)New York:Am. Inst. Phys.), 374, 172

Ramaty, R., Mandzhavidze, N., Kozlovsky, B., & Murphy, R. J 1995, ApJ, 455, L193

Ramaty, R., Mandzhavidze, N., Kozlovsky, B., & Skibo, J. G 1993, Adv. Sp. Res., 15, No. 7, 41

Ramaty, R., Schwartz, R. A., Enome, S., & Nakajima, H 1994, ApJ, 436, 941

Rank, G. 1995, Ph.D. thesis, Max Plank Inst

Rank, G., Bennet, K., Bloemen, H., Debrunner, H., Lockwood, J., McConnell, M., Ryan, J., Schonfelder, V., and Suleiman, R. 1996, in High Energy Solar Physics, ed. R. Ramaty, N. Mandzhavidze, & X.-M. Hua (New York:Am. Inst. Phys.), 374, 219

Rank, G. Debrunner, H., Lockwood, J., McConnell, M., Ryan, J., and Schonfelder, V. 1997, 25th Internat. Coosmic-Ray Conf. (Durban), 1, 5

Reames, D. V., 1995, Adv. Sp. Res., 15, No. 7, 41

Rieger, E. 1994, ApJ, 90, 645

Rieger, E., & Marschhauser, H. 1990, in MAX '91 Workshop #3, Estes Park, CO, ed. R. Winglee, A. Kiplinger (Boulder:University of Colorado), 68

Share, G. H. 1996, private communication

Share G. H., & Murphy, R. J. 1995, ApJ, 452, 933

Share G. H., & Murphy, R. J. 1997a, ApJ, 485, 409

Share G. H., & Murphy, R. J. 1997b, ApJ, 484, L165

Simnett, G. M. 1995, Sp. Sci. Rev., 73, 387

Simnett, G. M., Share, G. H., Messina, D. C., Chupp, E. L., Forrest, D. J., & Rieger, E. 1986, Adv. Sp. Res., 6, No. 6, 105

Struminsky, A., Matsuoka, M., & Takahashi, K. 1994, ApJ, 429, 400

Temerin, M., & Roth, I. 1992, ApJ, 391, L105

Takahashi, K., Sakamoto, T., Matsuoka, M., Nishi, K., Yamada, Y., Shimoda, S., Shikata, T., Wada, M., KuSunose, M., Yoshimori, M., & Kondo, I. 1991, 22nd Internat. Cosmic-Ray Conf. (Dublin), 3, 37

Van Allen, J. A. 1993, Geophys. Res. Letters, 20, 2729

Vestrand, W. T., *et al.* 1997, *SMM*/GRS flare catalogue, in preparation

Vilmer, N. 1994, ApJS, 90, 611

Wang, H. T., & Ramaty R. 1974, Sol. Phys., 36, 129

Webber, W. R., & Lockwood, J. A. 1993, J. Geophys. Res., 98, 7821

Yoshimori, M. 1989, Sp. Sci. Rev., 51, 85

Yoshimori, M. 1994, ApJS, 90, 639

Line Energy (MeV)	*CGRO*/OSSE 1991 June 4	*SMM*/GRS 19-Flare Average[2]
1.24	0.35±0.07	0.30±0.03
1.37	0.77±0.09	0.77±0.04
1.63	1.26±0.07	1.36±0.05
1.78	0.60±0.06	0.49±0.04
4.44	1.47±0.06	1.10±0.04
∼5.4	0.07±0.03	0.26±0.02
6.13	≡1.00±0.05	≡1.00±0.03
∼7	0.95±0.06	0.56±0.02

Table 1: Relative Narrow-Line Fluxes[1]

[1]The line fluxes are normalized to that of the 6.129 MeV ^{16}O line.

[2]From Share and Murphy (1995)

	B(G)		
s_e	100	200	300
2	1180	280	140
2.5	560	120	53
3	340	65	26
4	220	32	10
5	260	26	8

Table 2: Electron Trapping Times (s)

Fig. 1.— Rates observed in various X-ray and γ-ray bands from the 1991 June 4 solar flare. The dotted lines indicate the peak of the γ-ray emission and the end of the first-orbit observation by OSSE. Also plotted is the *GOES* 1 – 8 Å X-ray profile which saturated prior to the peak. Saturation effects were observed in all OSSE rates except that of the >16 MeV data.

Fig. 2.— The OSSE instrument.

Fig. 3.— Detector 2 response to a unit flux of 6 MeV photons for a source on axis (solid curve) and for a source 4.5° off-axis (dotted curve).

Fig. 4.— Count spectra and best fits obtained using the photon models described in the text. Panel (a) is an 8-s spectrum accumulated soon after the peak of emission in the first orbit by Detector 2 while pointing 4.5° off the Sun. The spectrum has been rebinned into larger energy intervals to improve the statistics for fitting. Panel (b) is a 2-min spectrum accumulated late in the first orbit by Detector 1 while pointing at the Sun. For display purposes, the data of this latter spectrum have been rebinned into slightly larger energy channels than those used in the fits.

Fig. 5.— High resolution time profile of the OSSE best-fitting photon spectra convolved with the BATSE Charged Particle Detector (CPD) response function (thick histogram). This is compared with the average observed BATSE count-rate from the four Sunward-facing CPDs (thin histogram). The 1-s BATSE count rates have been rebinned into the corresponding OSSE accumulation intervals. Also shown is the convolved OSSE flux increased by a factor of 2.5 (dotted histogram) to normalize it to the rising and falling portions of the observed BATSE count rate.

Fig. 6.— Time profile of the summed flux in narrow nuclear lines during three orbits of observations (histogram). Overplotted are the fluxes rebinned into the larger accumulation intervals as described in the text. Filled diamonds are from off-pointed data and open diamonds are from Sun-pointed data.

Fig. 7.— Low FIP-to-high FIP line flux ratio for the 19 *SMM*/GRS flares (Share 1996, private communication) compared with the OSSE June 4 ratios obtained for the first and second orbits and the mean for both orbits.

Fig. 8.— Time profile of the summed low-FIP to summed high-FIP line flux ratio derived from off-pointed (filled diamonds) and Sun-pointed (open diamonds) detector data. A straight line fit to the data is also shown.

Fig. 9.— Time profile of the summed low-FIP to 1.634 MeV Ne line flux ratio derived from

off-pointed (filled diamonds) and Sun-pointed (open diamonds) detector data.

Fig. 10.— Time profile of the accelerated proton power law spectral index derived from the 6.129-to-1.634 O/Ne line flux ratio obtained from off-pointed (filled diamonds) and Sun-pointed (open diamonds) detector data.

Fig. 11.— Time profile of the instantaneous power in accelerated protons obtained from off-pointed (filled diamonds) and Sun-pointed (open diamonds) detector data.

Fig. 12.— Time profile of the >1 MeV bremsstrahlung flux obtained from off-pointed (filled diamonds) and Sun-pointed (open diamonds) detector data. The first-orbit Sun-pointed data point has been shifted in time for display purposes.

Fig. 13.— Time profile of the instantaneous power in accelerated >0.1 MeV electrons obtained from off-pointed (filled diamonds) and Sun-pointed (open diamonds) detector data. The first-orbit Sun-pointed data point has been shifted in time for display purposes.

Fig. 14.— Panel a: High resolution time profile of the >1 MeV bremsstrahlung and the summed high-FIP line flux obtained from off-pointed detector data during the first orbit. The data have been rebinned into larger accumulation intervals and a correction has been applied to the flux values during the 16 seconds at the peak to account for saturation. The high-FIP flux has been multiplied by a factor of 300 for clarity. Also shown are the 80 GHz Nobeyama radio data (Ramaty *et al.* 1994; Enome 1995, private communication) normalized to the rising and falling portions of the bremsstrahlung and the Ulysses >0.025 MeV count rate (Kane *et al.* 1997) with arbitrary normalization. Panel b: Detail of the peak of the flare showing the >1 MeV bremsstrahlung, the 80 GHz Nobeyama radio data, the background-subtracted >16 MeV OSSE flux (DelSignore 1995), and the BATSE CPD count rate. The BATSE CPD and the 80 GHz emission have been normalized to the rising and falling portions of the bremsstrahlung. The >16 MeV flux has been renormalized to have a flux similar to that of the bremsstrahlung at the peak.

Fig. 15.— High resolution time profiles (histograms) of the 2.223 MeV neutron-capture line flux (Panel a) and the summed flux of narrow nuclear lines from high-FIP elements (at 1.634, 4.439, 6.129 and 6.99 MeV; Panel b) during the first orbit. A factor of 2 has been applied to the flux values during the 16 seconds at the peak to account for saturation effects. Also shown in Panel a are the EGRET/TASC 2.223 MeV line data (Bertsch *et al.* 1997).

Fig. 16.— The predicted time profile of the neutron capture line compared with the data. The dotted envelope represents the $\pm 1\sigma$ uncertainties.

Fig. 17.— Time profile of the 2.223 MeV neutron-capture line during three orbits of

observations (histogram). Also shown are the 80 GHz Nobeyama radio data (Ramaty *et al.* 1994; Enome 1995, private communication).

Fig. 18.— Time profile of the 2.223 MeV neutron-capture line derived from fits to data obtained using standard OSSE background subtraction techniques for several orbits around the June 4 X12+ orbit. Also shown is the *GOES* 1 – 8 Å flux.

Fig. 19.— Time profile of the flux ratio of >1 MeV bremsstrahlung to high-FIP lines obtained from off-pointed (filled diamonds) and Sun-pointed (open diamonds) detector data. The first-orbit Sun-pointed data point has been shifted in time for display purposes.

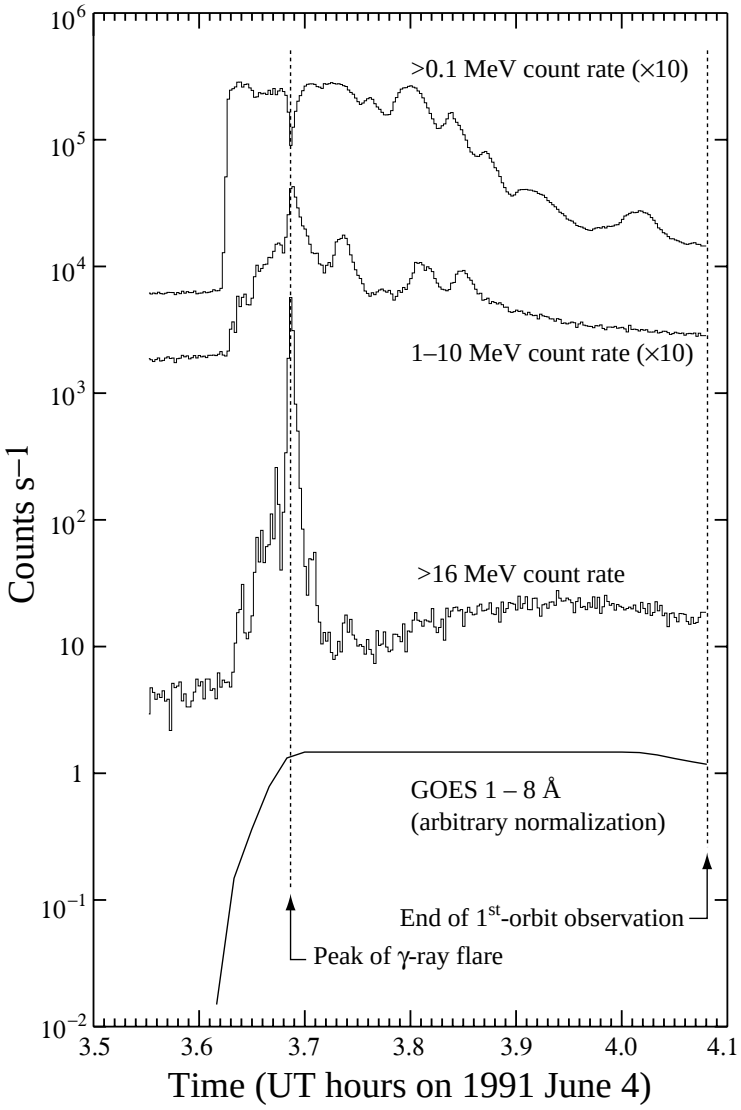
>0.1 MeV count rate (×10)
1–10 MeV count rate (×10)
>16 MeV count rate
GOES 1 – 8 Å
(arbitrary normalization)
End of 1st-orbit observation
Peak of γ-ray flare
Counts s−1
Time (UT hours on 1991 June 4)

Figure 1

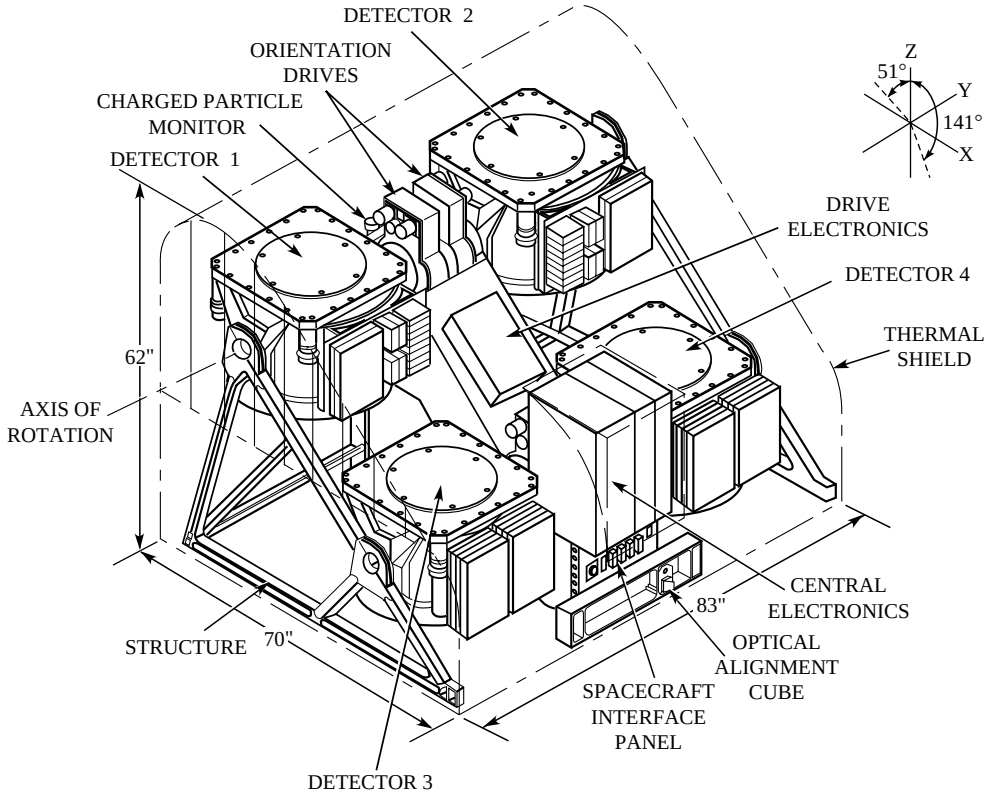
DETECTOR 2
ORIENTATION DRIVES
CHARGED PARTICLE MONITOR
DETECTOR 1
Z
51°
Y
141°
X
DRIVE ELECTRONICS
DETECTOR 4
THERMAL SHIELD
62"
AXIS OF ROTATION
CENTRAL ELECTRONICS
83"
STRUCTURE
70"
OPTICAL ALIGNMENT CUBE
SPACECRAFT INTERFACE PANEL
DETECTOR 3

Figure 2

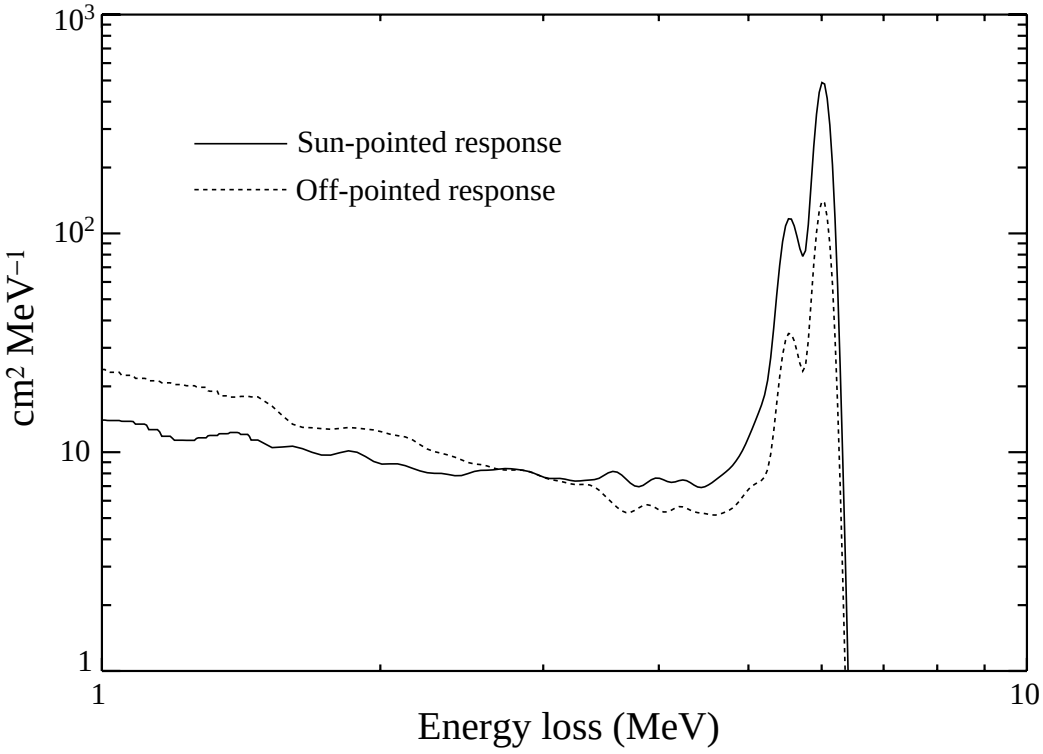
10^3
10^2
10
1
1
10
cm^2 MeV^{-1}
Energy loss (MeV)
Sun-pointed response
Off-pointed response

Figure 3

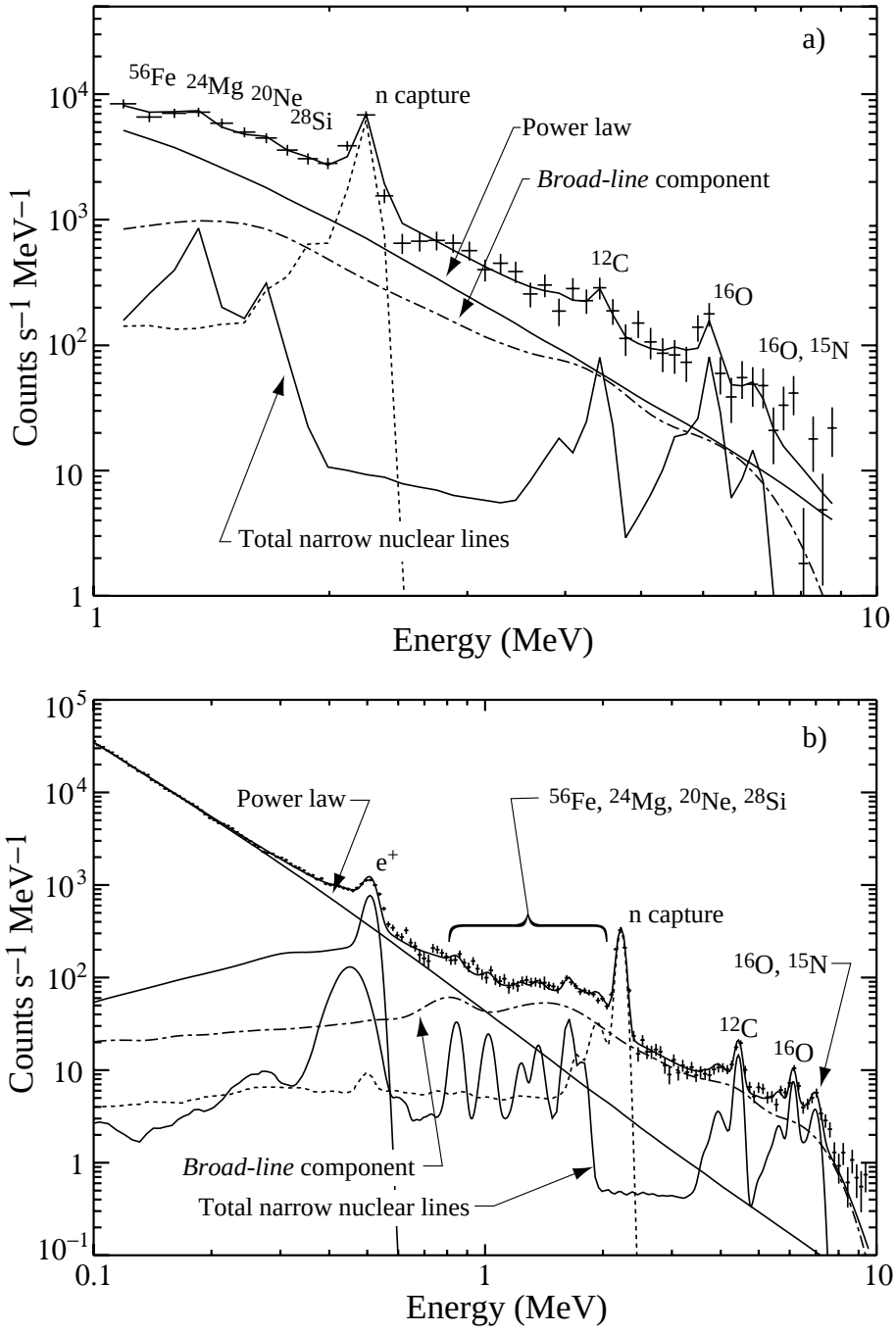
a)
^{56}Fe ^{24}Mg ^{20}Ne ^{28}Si
n capture
Power law
Broad-line component
^{12}C
^{16}O
^{16}O, ^{15}N
Total narrow nuclear lines
Counts s^{-1} MeV^{-1}
Energy (MeV)
b)
Power law
e^{+}
^{56}Fe, ^{24}Mg, ^{20}Ne, ^{28}Si
n capture
^{16}O, ^{15}N
^{12}C
^{16}O
Broad-line component
Total narrow nuclear lines
Counts s^{-1} MeV^{-1}
Energy (MeV)

Figure 4

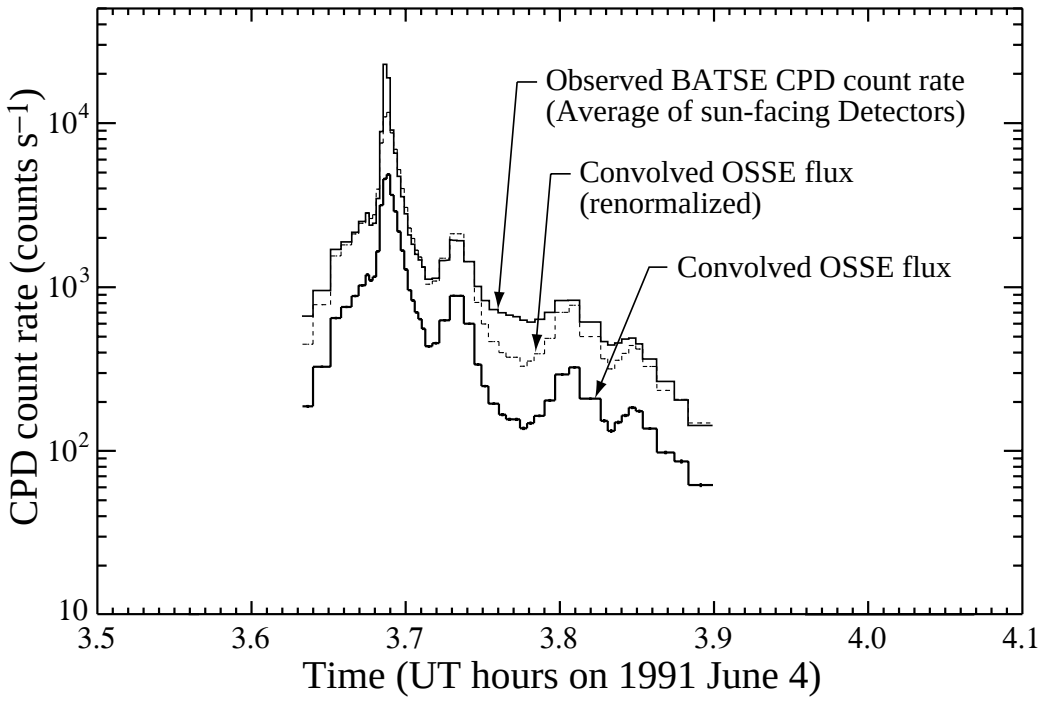
Observed BATSE CPD count rate
(Average of sun-facing Detectors)
Convolved OSSE flux
(renormalized)
Convolved OSSE flux
CPD count rate (counts s^{-1})
10^4
10^3
10^2
10
3.5
3.6
3.7
3.8
3.9
4.0
4.1
Time (UT hours on 1991 June 4)

Figure 5

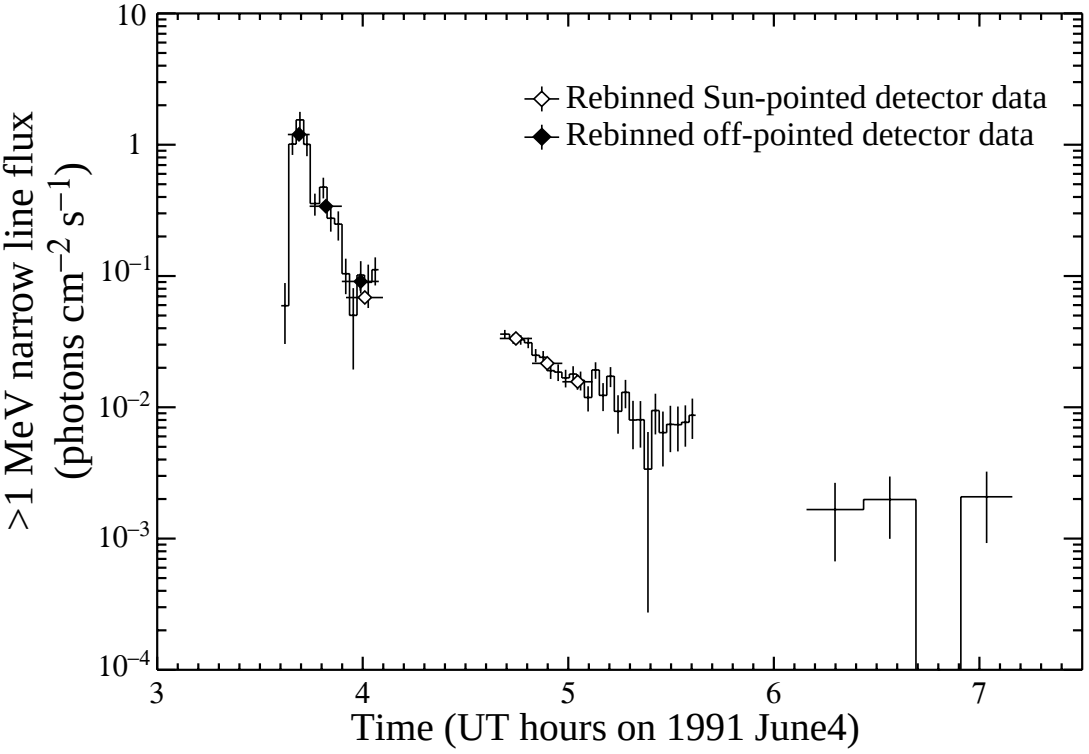
Rebinned Sun-pointed detector data
Rebinned off-pointed detector data
>1 MeV narrow line flux
(photons cm^{-2} s^{-1})
Time (UT hours on 1991 June4)
10
1
10^{-1}
10^{-2}
10^{-3}
10^{-4}
3
4
5
6
7

Figure 6

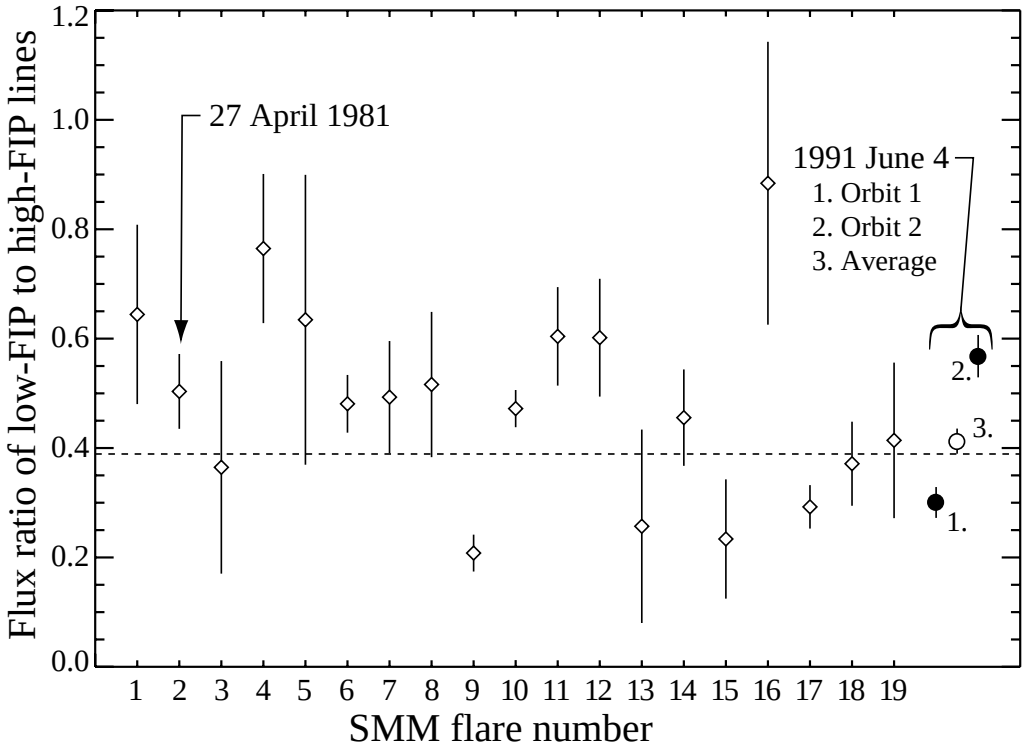
Flux ratio of low-FIP to high-FIP lines
1.2
1.0
0.8
0.6
0.4
0.2
0.0
27 April 1981
1991 June 4
1. Orbit 1
2. Orbit 2
3. Average
2.
3.
1.
1 2 3 4 5 6 7 8 9 10 11 12 13 14 15 16 17 18 19
SMM flare number

Figure 7

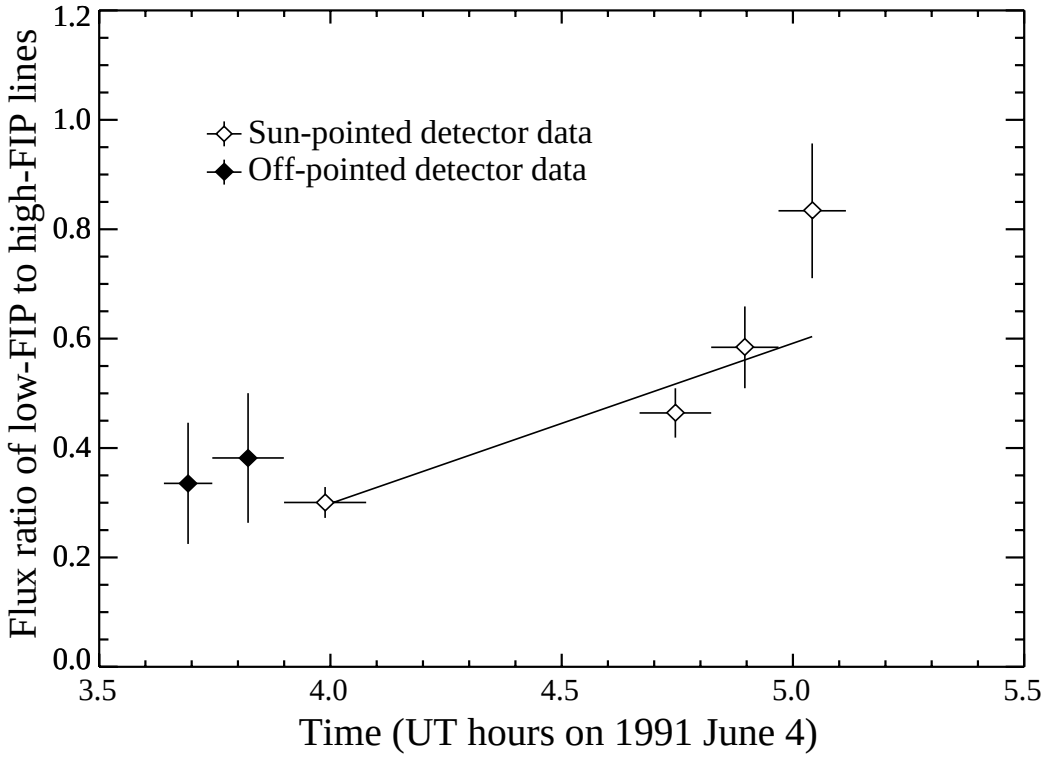
Flux ratio of low-FIP to high-FIP lines
Time (UT hours on 1991 June 4)
Sun-pointed detector data
Off-pointed detector data
0.0
0.2
0.4
0.6
0.8
1.0
1.2
3.5
4.0
4.5
5.0
5.5

Figure 8

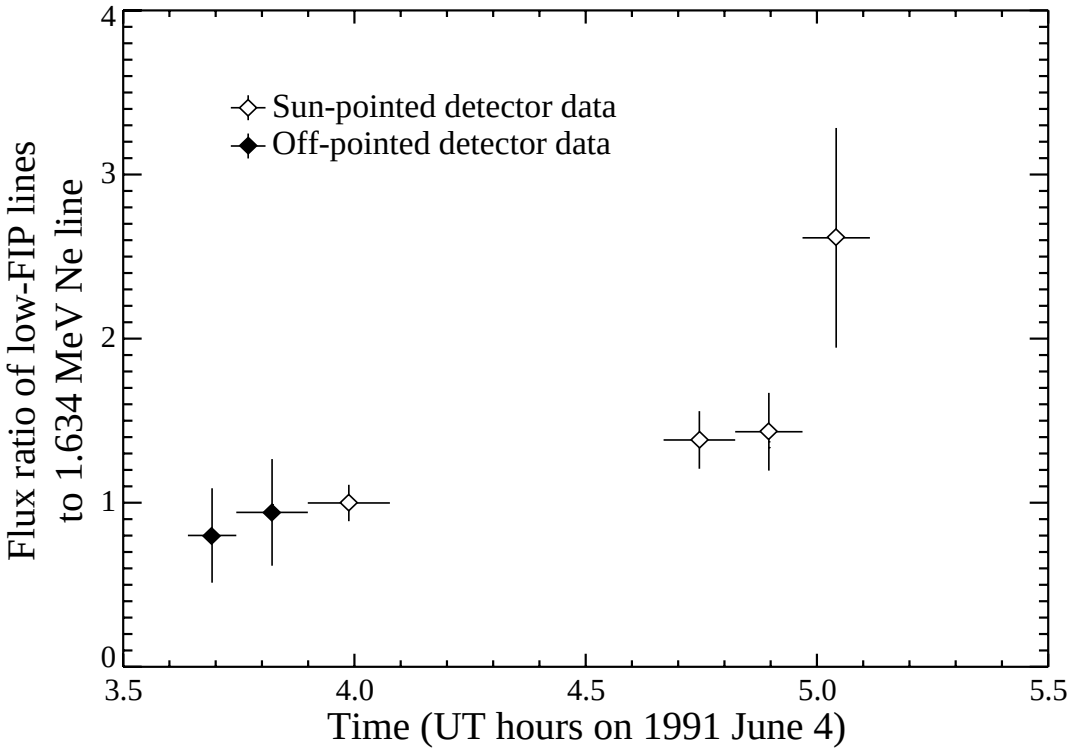
Sun-pointed detector data
Off-pointed detector data
Flux ratio of low-FIP lines
to 1.634 MeV Ne line
Time (UT hours on 1991 June 4)
0
1
2
3
4
3.5
4.0
4.5
5.0
5.5

Figure 9

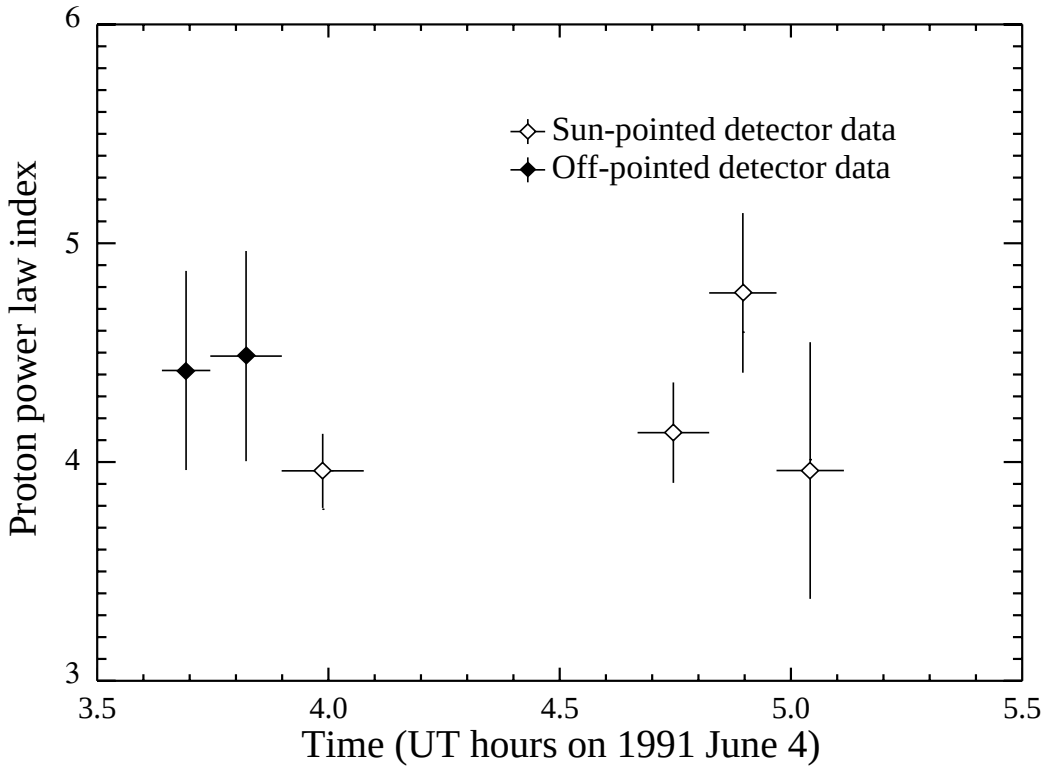
Sun-pointed detector data
Off-pointed detector data
Proton power law index
Time (UT hours on 1991 June 4)
6
5
4
3
3.5
4.0
4.5
5.0
5.5

Figure 10

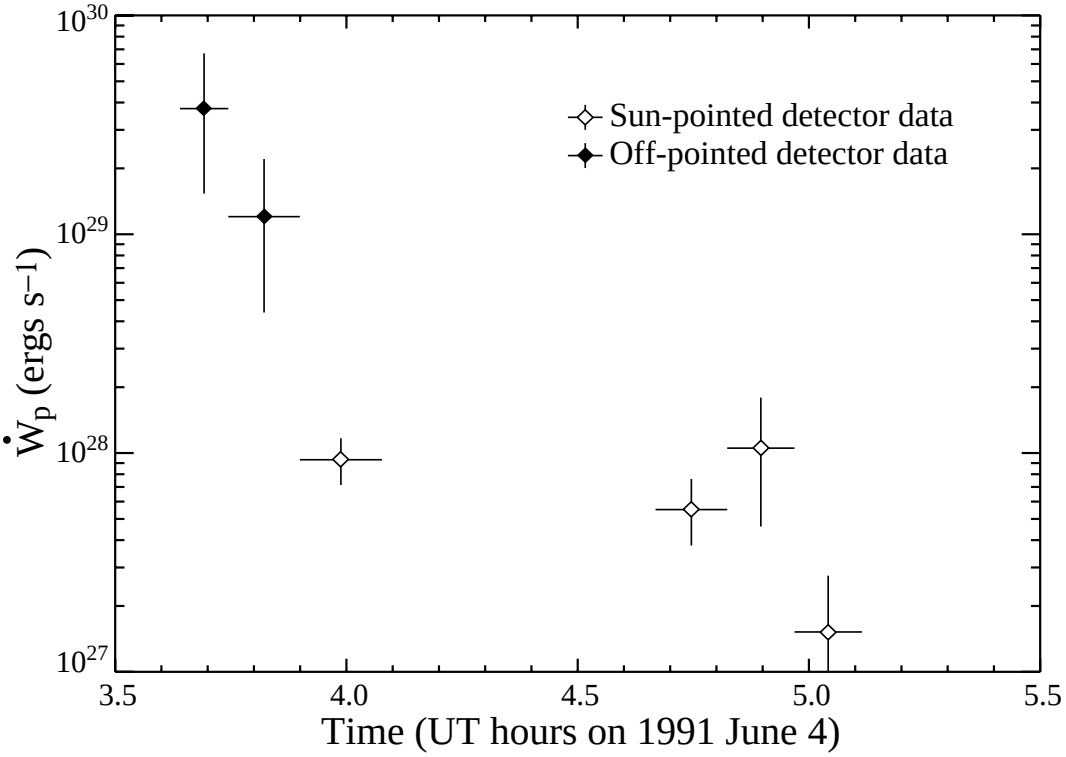
10^{30}
10^{29}
10^{28}
10^{27}
$\dot{W}_p$ (ergs s^{-1})
Sun-pointed detector data
Off-pointed detector data
3.5
4.0
4.5
5.0
5.5
Time (UT hours on 1991 June 4)

Figure 11

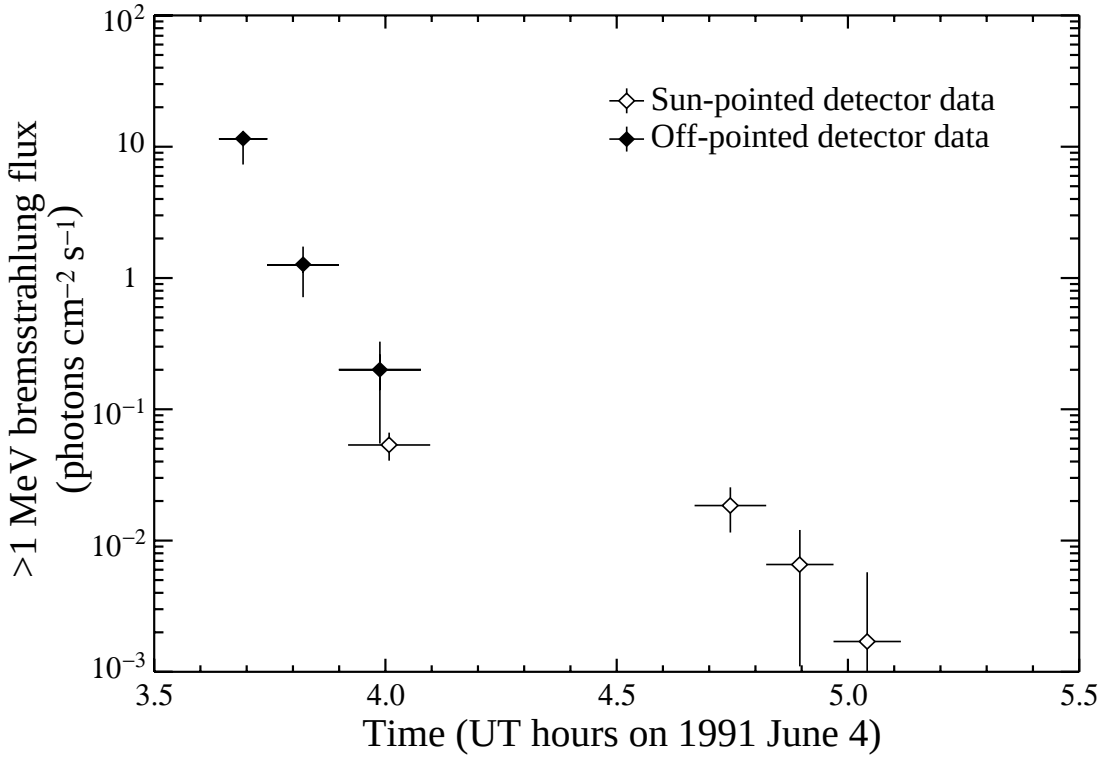
Sun-pointed detector data
Off-pointed detector data
>1 MeV bremsstrahlung flux
(photons cm^{-2} s^{-1})
Time (UT hours on 1991 June 4)
10^2
10
1
10^{-1}
10^{-2}
10^{-3}
3.5
4.0
4.5
5.0
5.5

Figure 12

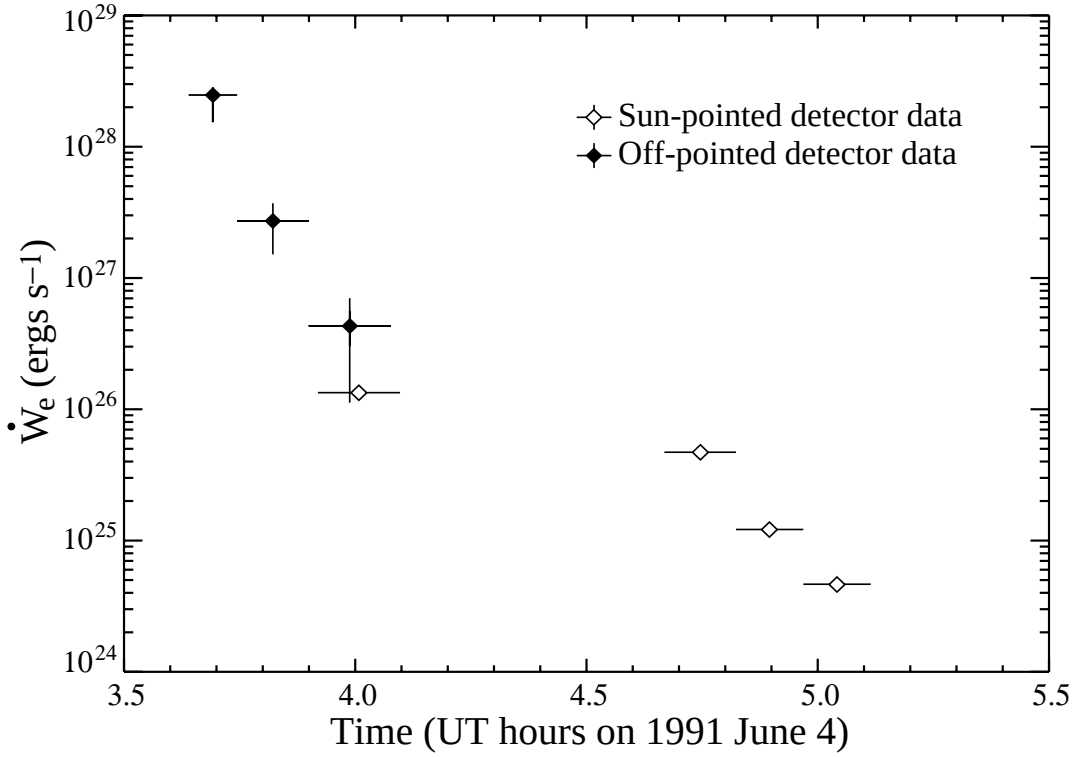
10^{29}
10^{28}
10^{27}
10^{26}
10^{25}
10^{24}
$\dot{W}_e$ (ergs s^{-1})
Sun-pointed detector data
Off-pointed detector data
3.5
4.0
4.5
5.0
5.5
Time (UT hours on 1991 June 4)

Figure 13

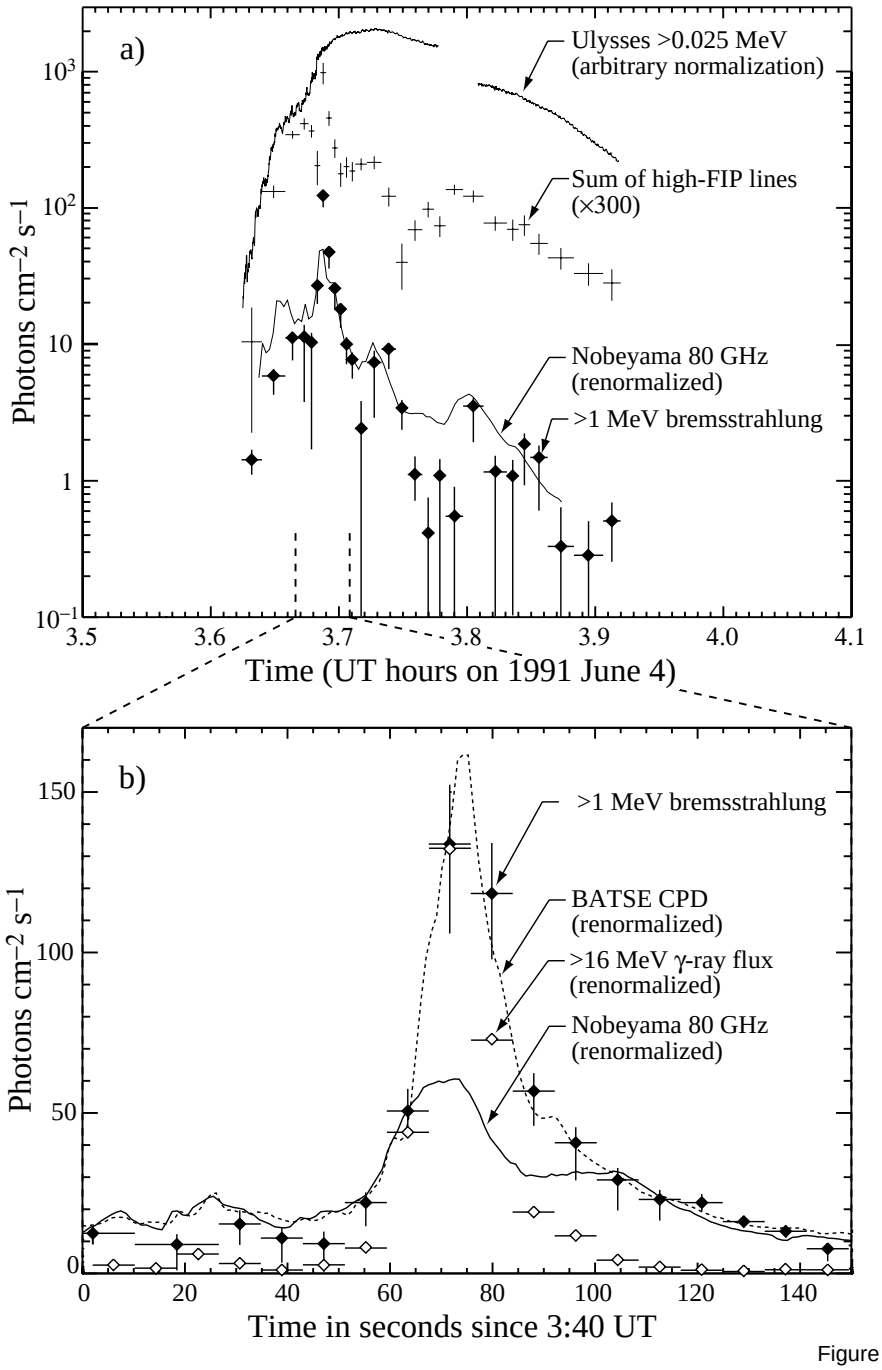
a)
Ulysses >0.025 MeV
(arbitrary normalization)
Sum of high-FIP lines
(×300)
Nobeyama 80 GHz
(renormalized)
>1 MeV bremsstrahlung
Photons cm^{-2} s^{-1}
Time (UT hours on 1991 June 4)
b)
>1 MeV bremsstrahlung
BATSE CPD
(renormalized)
>16 MeV γ-ray flux
(renormalized)
Nobeyama 80 GHz
(renormalized)
Photons cm^{-2} s^{-1}
Time in seconds since 3:40 UT

Figure 14

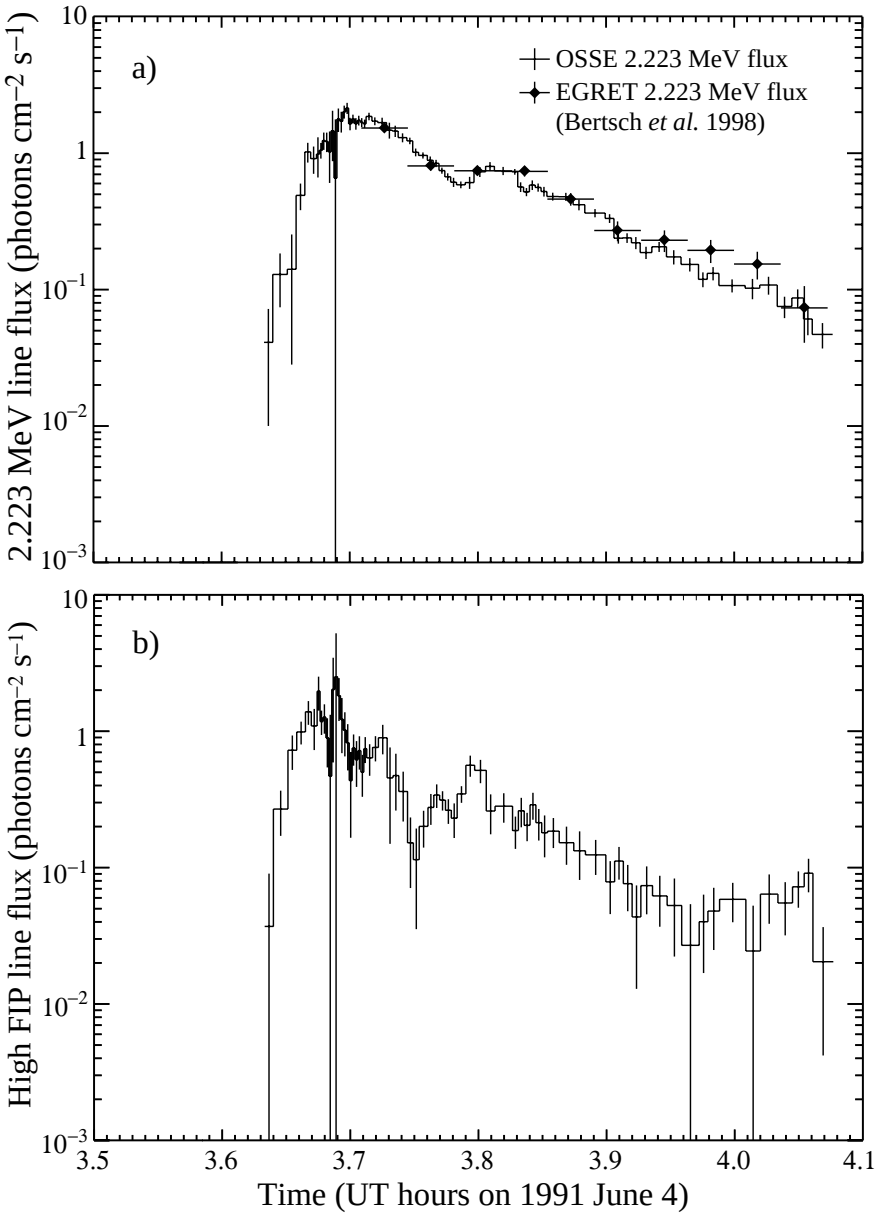
a)
OSSE 2.223 MeV flux
EGRET 2.223 MeV flux
(Bertsch *et al.* 1998)
2.223 MeV line flux (photons cm^{-2} s^{-1})
b)
High FIP line flux (photons cm^{-2} s^{-1})
Time (UT hours on 1991 June 4)

Figure 15

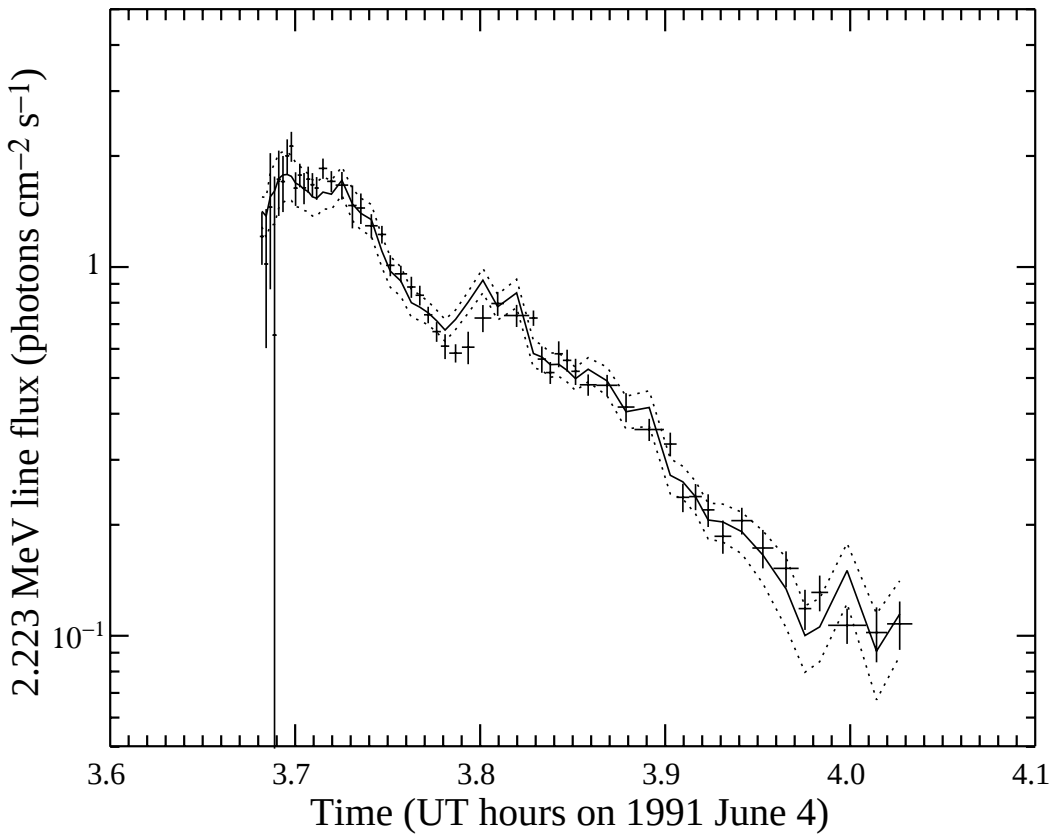
2.223 MeV line flux (photons cm^{-2} s^{-1})
1
10^{-1}
3.6
3.7
3.8
3.9
4.0
4.1
Time (UT hours on 1991 June 4)

Figure 16

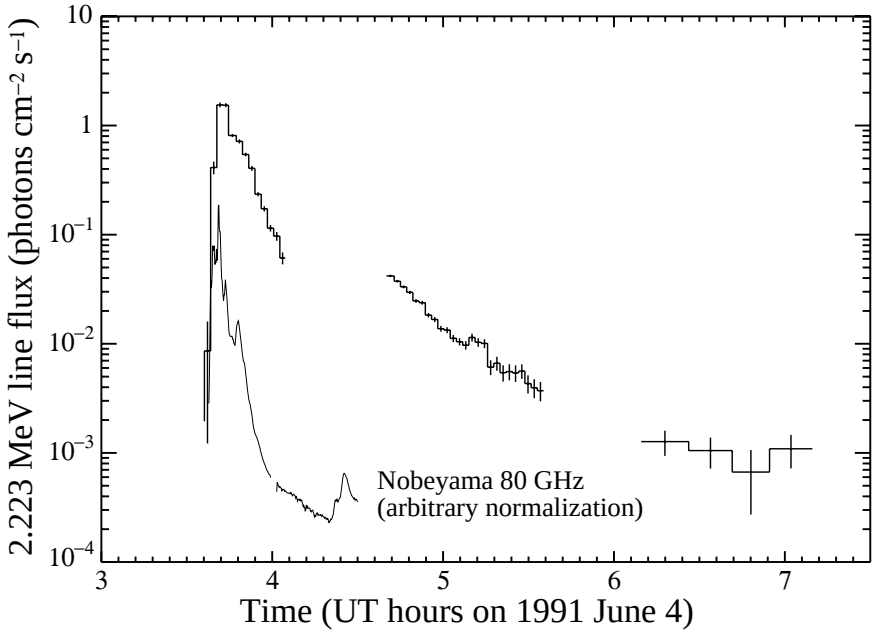
2.223 MeV line flux (photons cm^{-2} s^{-1})
10
1
10^{-1}
10^{-2}
10^{-3}
10^{-4}
3
4
5
6
7
Time (UT hours on 1991 June 4)
Nobeyama 80 GHz
(arbitrary normalization)

Figure 17

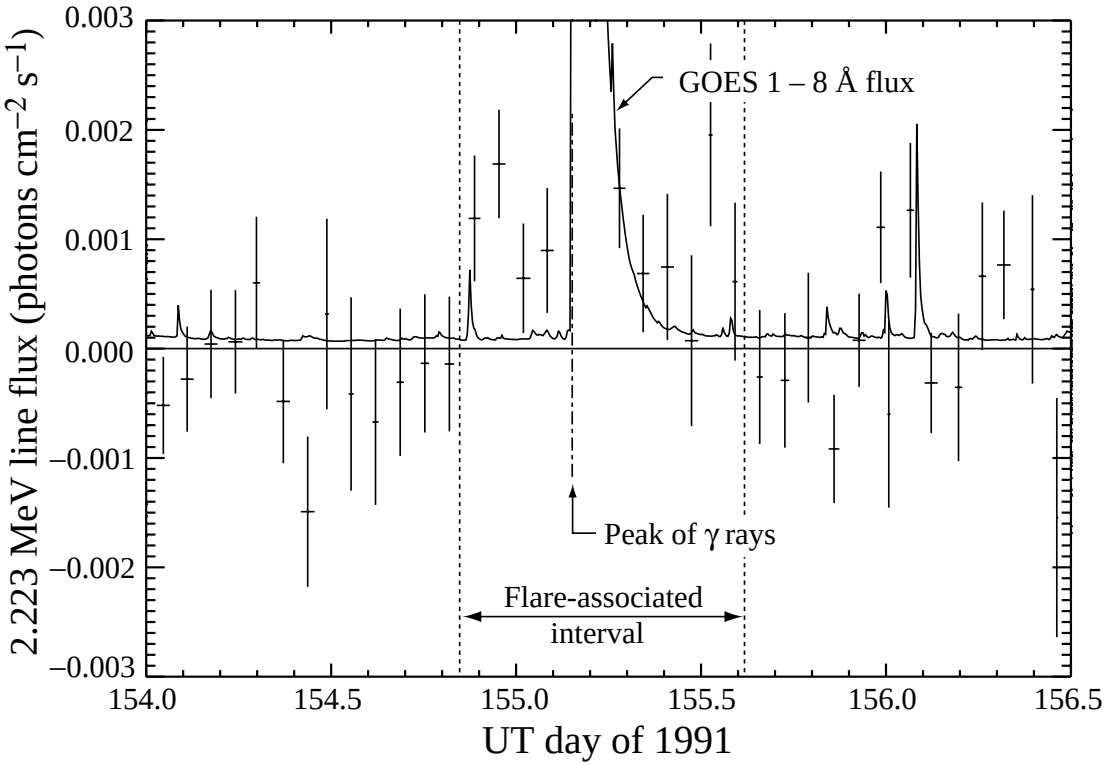
0.003
0.002
0.001
0.000
–0.001
–0.002
–0.003
2.223 MeV line flux (photons cm^{-2} s^{-1})
GOES 1 – 8 Å flux
Peak of γ rays
Flare-associated
interval
154.0
154.5
155.0
155.5
156.0
156.5
UT day of 1991

Figure 18

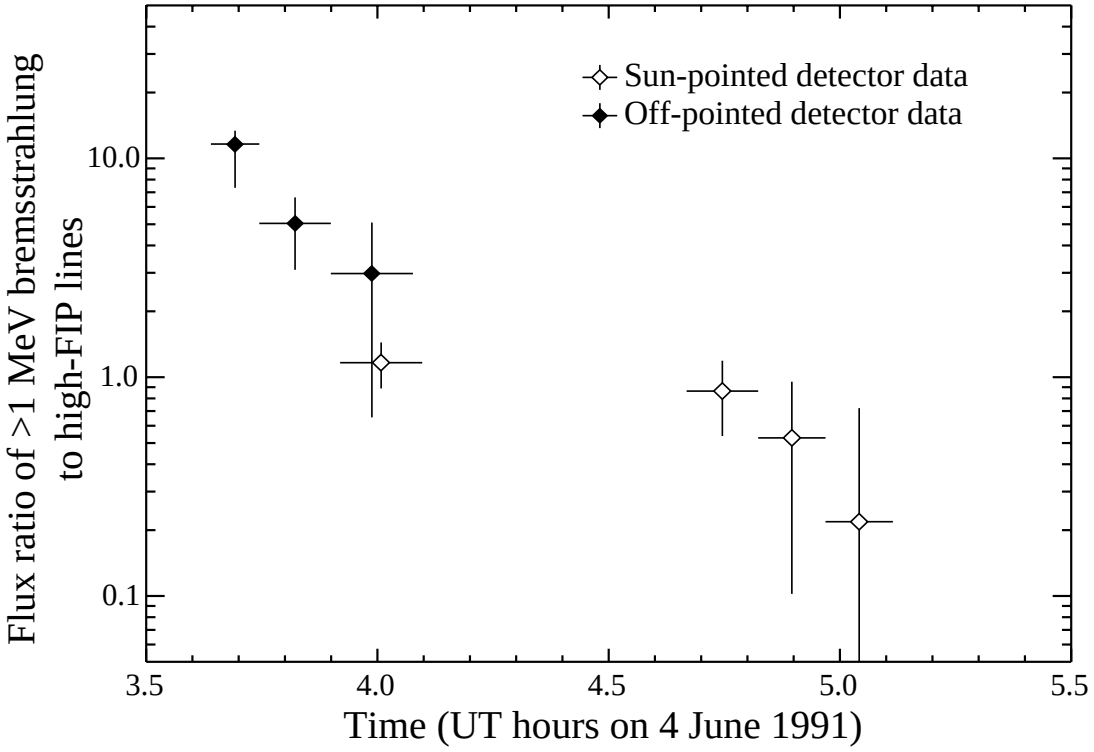
Sun-pointed detector data
Off-pointed detector data
Flux ratio of >1 MeV bremsstrahlung to high-FIP lines
10.0
1.0
0.1
3.5
4.0
4.5
5.0
5.5
Time (UT hours on 4 June 1991)

Figure 19